

AFRL-SN-WP-TP-2005-1163



**AEROSPACE SENSOR COMPONENT AND
SUBSYSTEM INVESTIGATION AND
INNOVATION-2 COMPONENT EXPLORATION
AND DEVELOPMENT (ASCSII-2 CED)**

**Delivery Order 0002: Volume 2 – Reconfigurable Aperture Antenna Virtual
Prototyping (Wideband Lumped Circuit Models For Integrated Spiral
Inductors)**

**Andrew W. Buurma and Roberto G. Rojas
The Ohio State University
ElectroScience Laboratory
Department of Electrical and Computer Engineer
1320 Kinnear Road
Columbus, OH 43212**

**Systran Federal Corp.
4027 Colonel Glenn Highway, Suite 210
Dayton, OH 45431-1672**

SEPTEMBER 2005

Final Report for 30 March 2001 – 31 Mar 2005

Approved for public release; distribution is unlimited.

STINFO FINAL REPORT

**SENSORS DIRECTORATE
AIR FORCE RESEARCH LABORATORY
AIR FORCE MATERIEL COMMAND
WRIGHT-PATTERSON AIR FORCE BASE, OH 45433-7320**

NOTICE

Using Government drawings, specifications, or other data included in this document for any purpose other than Government procurement does not in any way obligate the U.S. Government. The fact that the Government formulated or supplied the drawings, specifications, or other data does not license the holder or any other person or corporation; or convey any rights or permission to manufacture, use, or sell any patented invention that may relate to them.

This report was cleared for public release by the Air Force Research Laboratory Wright Site (AFRL/WS) Public Affairs Office (PAO) and is releasable to the National Technical Information Service (NTIS). It will be available to the general public, including foreign nationals.

PAO Case Number: AFRL/WS-05-2479, 25 Oct 05

THIS TECHNICAL REPORT IS APPROVED FOR PUBLICATION.

//S//
[signature of project monitor/in-house author]

//S//
[signature of supervisor]

//S//
[signature of three letter chief]

This report is published in the interest of scientific and technical information exchange and its publication does not constitute the Government's approval or disapproval of its ideas or findings.

REPORT DOCUMENTATION PAGE				Form Approved OMB No. 0704-0188	
Public reporting burden for this collection of information is estimated to average 1 hour per response, including the time for reviewing instructions, searching existing data sources, gathering and maintaining the data needed, and completing and reviewing this collection of information. Send comments regarding this burden estimate or any other aspect of this collection of information, including suggestions for reducing this burden to Department of Defense, Washington Headquarters Services, Directorate for Information Operations and Reports (0704-0188), 1215 Jefferson Davis Highway, Suite 1204, Arlington, VA 22202-4302. Respondents should be aware that notwithstanding any other provision of law, no person shall be subject to any penalty for failing to comply with a collection of information if it does not display a currently valid OMB control number. PLEASE DO NOT RETURN YOUR FORM TO THE ABOVE ADDRESS.					
1. REPORT DATE (DD-MM-YYYY) September 2005		2. REPORT TYPE Final		3. DATES COVERED (From - To) 30 Mar 2001 – 31 Mar 2005	
4. TITLE AND SUBTITLE Aerospace Sensor Component And Subsystem Investigation And Innovation-2 Component Exploration And Development (ASCI-2 CED) Delivery Order 0002: Volume 2 – Reconfigurable Aperture Antenna Virtual Prototyping (Wideband Lumped Circuit Models For Integrated Spiral Inductors)				5a. CONTRACT NUMBER F33615-00-D-1726-0002	
				5b. GRANT NUMBER	
				5c. PROGRAM ELEMENT NUMBER 62204F	
6. AUTHOR(S) Andrew W. Buurma and Roberto G. Rojas (Ohio State University)				5d. PROJECT NUMBER 2002	
				5e. TASK NUMBER 06	
				5f. WORK UNIT NUMBER 08	
7. PERFORMING ORGANIZATION NAME(S) AND ADDRESS(ES) Systran Federal Corp. 4027 Colonel Glenn Highway, Suite 210 Dayton, OH 45431-1672				8. PERFORMING ORGANIZATION REPORT NUMBER	
The Ohio State University ElectroScience Laboratory Dept of Electrical & Computer Engineer 1320 Kinnear Road Columbus, OH 43212					
9. SPONSORING / MONITORING AGENCY NAME(S) AND ADDRESS(ES) SENSORS DIRECTORATE AIR FORCE RESEARCH LABORATORY AIR FORCE MATERIEL COMMAND WRIGHT-PATTERSON AFB, OH 45433-7320				10. SPONSOR/MONITOR'S ACRONYM(S) AFRL/SNDM	
				11. SPONSOR/MONITOR'S REPORT NUMBER(S) AFRL-SN-WP-TP-2005-1163	
12. DISTRIBUTION / AVAILABILITY STATEMENT Approved for public release; distribution unlimited.					
13. SUPPLEMENTARY NOTES See also Volume 1, AFRL-SN-WP-TR-2005-1162 and Volume 3, AFRL-SN-WP-TR-2005-1164. This report contains color.					
14. ABSTRACT <p>As the speed of transistors has risen in recent years, acquiring accurate models for the passive devices used in integrated circuits has become a greater challenge. Current device speeds are in the tens of GHz, and at these frequencies the parasitic effects of inductors can become difficult to predict. At GHz level frequencies, monolithic inductors suffer from severe parasitic effects. The relatively large size of the inductor (hundreds of microns), and the high dielectric constant of the substrate, cause the inductor to experience significant capacitive coupling. The skin effect, along with the fields coupling into a lossy substrate, causes the structures to dissipate a significant amount of power. Additionally, the effect of eddy currents must be understood as they too result in power loss. These parasitic effects result in a limited peak Q. Since many RF circuits such as LNA's and VCO's require inductors with a high Q, it is critical for the circuit designer to accurately model these parasitics.</p>					
15. SUBJECT TERMS: Lumped circuit models, RF circuits, Spiral inductors, monolithic inductors, capacitive coupling					
16. SECURITY CLASSIFICATION OF:			17. LIMITATION OF ABSTRACT SAR	18. NUMBER OF PAGES 54	19a. NAME OF RESPONSIBLE PERSON Gregory L. Creech
a. REPORT Unclassified	b. ABSTRACT Unclassified	c. THIS PAGE Unclassified			19b. TELEPHONE NUMBER (include area code) (937) 255-4831 X3486

Table of Contents

Chapter 1 Introduction	1
Chapter 2 Summary of the PEEC Distributed Circuit	2
2.1 Review of EM Equations	3
2.2 Discretizing the Inductor.....	5
2.3 Formulation of the PEEC System of Equations.....	6
2.4 Creating the Distributed Circuit from the System of Equations	9
Chapter 3 Calculating the Resistance Matrix.....	12
3.1 Eddy Currents in a Spiral Inductor	12
3.2 The Skin Effect	14
3.3 Calculating the Frequency Dependent Resistance	15
Chapter 4 Deriving the Inductor Lumped Pi-Model.....	17
4.1 First Low Frequency Approximation.....	19
4.2 Second Low Frequency Approximation	20
4.3 High Frequency Approximation	22
Chapter 5 Comparison with Momentum and Measured Data	25
5.1 Inductor Results	25
Chapter 6 Summary and Conclusions.....	32

List of Figures

Figure 1 - Flowchart showing the Distributed Model Derivation.....	2
Figure 2 - Profile of multi-layer substrate.....	4
Figure 3 - Discretization for 1.5 turn inductor.....	5
Figure 4 - Coordinate system used: (a) top view and (b) side view of substrate.....	5
Figure 5 - Equivalent KCL for three series rectangles	9
Figure 6 - Equivalent KCL with capacitors	10
Figure 7 - KVL circuit for one rectangle	10
Figure 8 - PEEC distributed circuit for three series rectangles.....	11
Figure 9 - Cross-section of a trace illustrating the total current distribution.....	12
Figure 10 - Coordinate system for the top view of a rectangle.....	13
Figure 11 - Cross-section of current distribution.....	14
Figure 12 - Inductor lumped pi-model derivation flowchart	17
Figure 13 - Inductor lumped pi-model.....	18
Figure 14 - Distributed circuit following a low frequency approximation.....	19
Figure 15 - Pi-circuit neglecting capacitances	19
Figure 16 - PEEC circuit after second low frequency approximation.....	20
Figure 17 - Low frequency pi-circuit with port 2 shorted	21
Figure 18 - High frequency approximation for four series rectangles.....	23
Figure 19 - Illustration of bridge overlap capacitance – 2.5 turn inductor	23
Figure 20 - Inductor voltage vs. Inductor rectangle for 1.5 turn inductor	24
Figure 21 - Inductor voltage vs. Inductor rectangle for 3.5 turn inductor	24
Figure 22 - ADS schematic for inductor #1.....	27
Figure 23 - 1.5 turn inductor (a) and open (b) test structure.....	27
Figure 24 - Simulated results inductor #1.....	29
Figure 25 - Simulated results inductor #2.....	29
Figure 26 - Simulated results inductor #3.....	30
Figure 27 - Simulated results inductor #4.....	30
Figure 28 - Simulated results inductor #5.....	31
Figure 29 - De-embedded measured results for inductor #1.....	31
Figure 30 - Profile of L-layered substrate.....	35
Figure 31 - Coordinates for rectangles i and j (based on [5])	43
Figure 32 - Unequal parallel filaments with offset	49
Figure 33 - Unequal parallel filaments with full overlap.....	49
Figure 34 - Unequal parallel filaments with no offset.....	50

Chapter 1 Introduction

As the speed of transistors has risen in recent years, acquiring accurate models for the passive devices used in integrated circuits has become a greater challenge. Current device speeds are in the tens of GHz, and at these frequencies the parasitic effects of inductors can become difficult to predict. At GHz level frequencies, monolithic inductors suffer from severe parasitic effects. The relatively large size of the inductor (hundreds of microns), and the high dielectric constant of the substrate, cause the inductor to experience significant capacitive coupling. The skin effect, along with the fields coupling into a lossy substrate, causes the structures to dissipate a significant amount of power. Additionally, the effect of eddy currents must be understood as they too result in power loss. These parasitic effects result in a limited peak Q . Since many RF circuits such as LNA's and VCO's require inductors with a high Q , it is critical for the circuit designer to accurately model these parasitics.

At present, the best way to model the parasitic effects of a monolithic inductor is to apply data fitting techniques to a lumped circuit model, or to use a numerical EM solver. Data fitting techniques require the inductor to be fabricated multiple times which is both time consuming and expensive. EM solvers such as FEM, MoM, and FDTD can be both time consuming and numerically unstable when simulating electrically small structures (inductors are much smaller than $\lambda/20$). Although new schemes have been developed to handle electrically small structures, numerical techniques are still time consuming.

There are techniques in the literature, such as in [17] that use microstrip transmission line approximations to develop general expressions for the inductance and Q of spiral inductors. Other techniques, like that of [1], [6], [8], [15], and [16], involve the development of approximated empirical or semi-analytical formulas. Unfortunately, as mentioned by [11], these formulas can sometimes give results with an error on the order of 20%.

In this report, we begin in Chapter 2 with a summary of the Partial Element Equivalent Circuit (PEEC) distributed circuit model for a spiral inductor. Chapter 3 will deal with the derivation of the frequency dependent resistance model that accounts for skin effect and eddy currents. In Chapter 4, we review the approximations made to simplify the Partial Element Equivalent Circuit (PEEC) model into a simple lumped pi-model. In Chapter 5, we will see that the lumped model can be evaluated fairly quickly and, as will be demonstrated, with great accuracy. We will summarize our results in Chapter 6.

Chapter 2 Summary of the PEEC Distributed Circuit

The PEEC technique has been thoroughly developed by [4] as a tool by which Maxwell's equations are used to construct a distributed circuit to model interconnects in digital and microwave circuits. As the construction of the PEEC distributed circuit for inductors is discussed in great detail in [1], [4] - [6], and [9], it is only briefly summarized here, with reference to [11]. A flowchart showing the progression from Maxwell's equations (with a quasistatic approximation) to a distributed model is given in Figure 1.

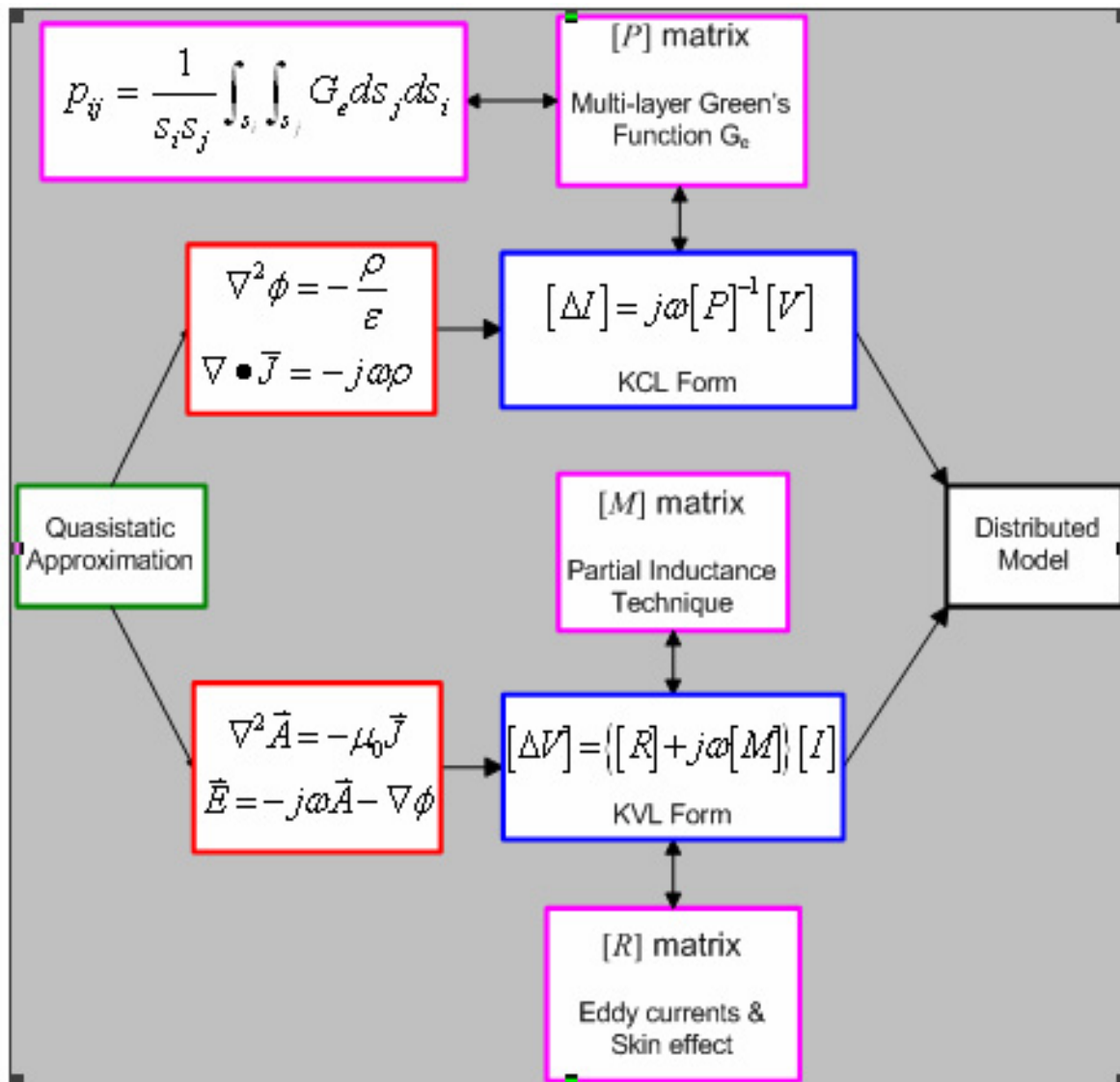


Figure 1 - Flowchart showing the Distributed Model Derivation

2.1 Review of EM Equations

Using Faraday's law in point form for the time periodic case concurrently with the constitutive relations for linear isotropic materials, one can arrive at the following expression for the electric field.

$$\vec{E} = -j\omega\vec{A} - \nabla\phi \quad (2.1)$$

Taking the divergence of both sides of equation (2.1) and applying the Lorenz gauge to the result will give

$$\nabla^2\phi + \omega^2\mu\varepsilon\phi = \frac{-\rho}{\varepsilon} \quad (2.2)$$

where ϕ is the scalar electric potential.

In a similar manner beginning from Ampere's law, we arrive at the magnetic equivalent to equation (2.2)

$$\nabla^2\vec{A} + \omega^2\mu\varepsilon\vec{A} = -\mu\vec{J}, \quad (2.3)$$

where \vec{A} is the vector magnetic potential. Since the devices we are studying are electrically very small, we can apply a quasi-static ($\omega \approx 0$) assumption to equation (2.2) and equation (2.3) which gives

$$\nabla^2\phi = -\frac{\rho}{\varepsilon} \quad (2.4)$$

$$\nabla^2\vec{A} = -\mu\vec{J} \quad (2.5)$$

Equation (2.5) is based upon the assumption that the substrate has very low loss. If we want to take into account losses in the substrate, we can use $\varepsilon_s = \varepsilon_0\varepsilon_{rs} - j\frac{\sigma_s}{\omega}$ in equation (2.3) to get (within the substrate)

$$\nabla^2\vec{A} + \omega^2\mu_0\left(\varepsilon_0\varepsilon_{rs} - j\frac{\sigma_s}{\omega}\right)\vec{A} = \nabla^2\vec{A} - j\omega\sigma_s\mu_0\vec{A} = -\mu\vec{J}, \quad (2.6)$$

where the ω^2 term is ignored because we are using a quasi-static approximation. The solution to equation (2.5) and equation (2.6), with the appropriate boundary conditions, is expressed in terms of the magnetostatic (G_m) Green's function.

$$\vec{A} = \int_v G_m \vec{J} dv \quad (2.7)$$

The solution for G_m for the lossless case (equation (2.5)) is simple because it does not involve the permittivity. Since the permeability of each layer of our substrate is the same as free space, G_m is simply the free space Green's function without the e^{-jBR} term, namely,

$$G_m(R) = \frac{\mu_0}{4\pi R}, \quad (2.8)$$

where R is the distance between the observation and source points. The solution to equation (2.6) (lossy case) is more involved and requires the application of appropriate boundary conditions to solve for a multi-layer G_m . That case will not be considered in this report. The solution to equation (2.4), with the appropriate boundary conditions, can be expressed in terms of the electrostatic (G_e) Green's function,

$$\phi = \int_v G_e \rho dv. \quad (2.9)$$

As mentioned previously, the inductors we are studying are electrically very small, making the use of static Green's functions appropriate. Following the method outlined in [5] and [10], G_e for the multi-layer substrate shown in Figure 2 is solved directly. The details of the derivation of the multilayer Green's function $G_e(\vec{r}, \vec{r}')$ are given in Appendix A.

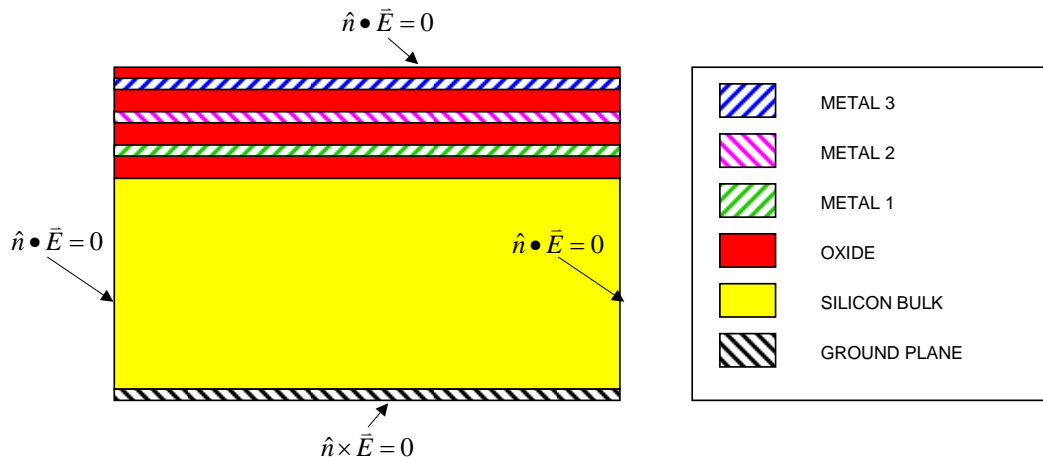


Figure 2 - Profile of multi-layer substrate

As will be discussed, equation (2.7) and equation (2.9) form the foundation for the system of equations that will be used to construct the PEEC distributed circuit.

2.2 Discretizing the Inductor

In general, the current and charge on a structure can be discretized any arbitrary way. In other words, the charge and current can be expressed in terms of a set of basis functions that is most appropriate for the geometry. However, for simplicity, as done in [11]-[13], the monolithic inductors are discretized into a set of series rectangles as illustrated in Figure 3. The coordinate system we use is shown in Figure 4.

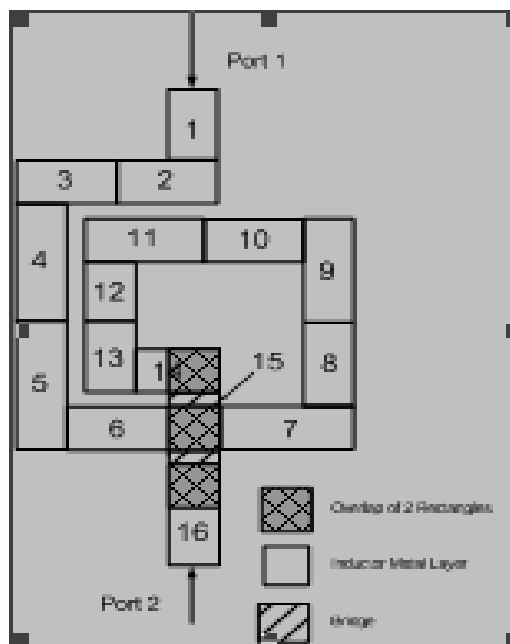


Figure 3 - Discretization for 1.5 turn inductor

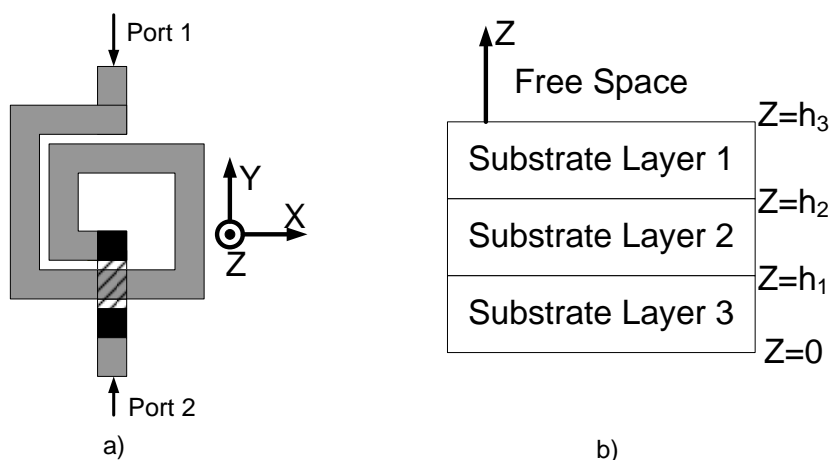


Figure 4 - Coordinate system used: (a) top view and (b) side view of substrate

The current and charge is then decomposed into a summation of pulse basis functions as done in [11]-[13]. The volume current density is given as

$$\vec{J}_i = \frac{I_i b(x, y, z)_i \hat{J}_i}{a_i}, \quad (2.10)$$

where $b(x, y, z)_i$ is a pulse function with a magnitude of 1 when the point (x, y, z) is inside rectangle i and is equal to zero; otherwise, \hat{J}_i is a unit vector that gives the direction of current flow and is always perpendicular to the cross-section into which it flows, whose area is denoted by a_i . I_i is a constant and represents the magnitude of the current. Similarly, the volume charge density in each segment is given as

$$\rho_i = \frac{Q_i b(x, y, z)_i}{v_i} \quad (2.11)$$

where $b(x, y, z)_i$ is the same as in equation (2.10), v_i is the volume of rectangle i , and Q_i is a constant that represents the total charge in the volume v_i . The total current and charge in the inductor is a summation of the individual basis functions. This gives the total current and charge density as

$$\vec{J} = \sum_{i=1}^N \vec{J}_i \quad (2.12)$$

$$\rho = \sum_{i=1}^N \rho_i \quad (2.13)$$

2.3 Formulation of the PEEC System of Equations

It is now possible to construct the PEEC distributed circuit with the equations we have derived up to this point. Plugging equation (2.7) into equation (2.1) and putting all terms to the right side will give

$$0 = \vec{E} + j\omega \int_v G_m \vec{J} dv + \nabla \phi. \quad (2.14)$$

We can replace \vec{J} in equation (2.14) with equation (2.10) and equation (2.12) to arrive at

$$0 = \vec{E} + j\omega \sum_{j=1}^N \frac{I_j}{a_j} \int_v G_m b(x, y, z)_j \hat{J}_j dv + \nabla \phi. \quad (2.15)$$

By defining the testing function to be the same as the basis function from equation (2.10), we can apply Galerkin's method and take the inner product of both sides of equation (2.15) with the testing function to arrive at

$$0 = \int_{v_i} \frac{\bar{E} \cdot \hat{J}_i dv_i}{a_i} + j\omega \sum_{j=1}^N \frac{I_j}{a_i a_j} \int_{v_i} \int_{v_j} G_m(\hat{J}_i \cdot \hat{J}_j) dv_j dv_i + \int_{v_i} \frac{\hat{J}_i \cdot \nabla \phi_i}{a_i} dv_i. \quad (2.16)$$

From the boundary condition on a good conductor, it can be shown that the first term on the right side of equation (2.16) represents the resistance ($1/\sigma$) of the inductor.

$$\bar{E} \cdot \hat{J}_i = \frac{|\bar{J}_i|}{\sigma}. \quad (2.17)$$

We call the double integral in the second term of equation (2.16) M_{ij} , the partial inductance matrix, namely,

$$M_{ij} = \frac{1}{a_i a_j} \int_{v_i} \int_{v_j} G_m(\hat{J}_i \cdot \hat{J}_j) dv_j dv_i, \quad (2.18)$$

where G_m was defined in equation (2.8). Plugging equation (2.8) into equation (2.18), we get

$$M_{ij} = \frac{\mu_0}{4\pi a_i a_j} \int_{a_i} \int_{l_i} \int_{a_j} \int_{l_j} \frac{d\hat{l}_i \cdot d\hat{l}_j}{|\bar{r}_i - \bar{r}_j|} da_i da_j. \quad (2.19)$$

The analytical solution to equation (2.19) can be very complicated. The techniques outlined in [2], [6], [7], and summarized in Appendix C, offer approximate solutions to equation (2.19) that give reasonable accuracy.

Finally, a finite difference approximation can be applied to the third term of equation (2.16) and simplify the equation to

$$0 = \frac{1}{a_i} \int_{v_i} R_s J_i dv_i + j\omega \sum_{j=1}^N I_j M_{ij} - \Delta V_i. \quad (2.20)$$

By definition, ΔV_i is the change in voltage from one end of rectangle i to the other end. As in [11]-[13], we define ΔV_i as

$$\Delta V_i = \phi(x_i^+, y_i^+, z_i^+) - \phi(x_i^-, y_i^-, z_i^-), \quad (2.21)$$

where $\phi(x_i^+, y_i^+, z_i^+)$ denotes the potential at the boundary between rectangle i and rectangle $i+1$. Similarly, $\phi(x_i^-, y_i^-, z_i^-)$ denotes the potential at the boundary between rectangle i and rectangle $i-1$. Expressing equation (2.20) in matrix form gives

$$[\Delta V] = ([R] + j\omega[M])[I]. \quad (2.22)$$

Whereas the system of equations expressed in equation (2.22) is based on equation (2.1) and equation (2.7), a second system of equations is generated from equation (2.9) and equation (2.23), the continuity equation.

$$\nabla \bullet \bar{J} = -j\omega\rho. \quad (2.23)$$

Similar to the application of Galerkin's method used in arriving at equation (2.16), we obtain equation (2.24).

$$V_i = \frac{1}{v_i} \int_{v_i} \phi_i dv_i = \sum_{j=1}^N \int_{v_i} \int_{v_j} \frac{Q_j}{v_i v_j} G_e dv_j dv_i. \quad (2.24)$$

Here, V_i is defined as the average potential on rectangle i . If we assume that the potential decreases linearly along the length of the rectangle, then V_i is approximately the potential at the center of the rectangle.

In using this technique for an N rectangle structure, there are two variables that are not assigned to rectangles, namely V_0 and V_{N+1} . However, the input and output ports of the inductor are located at the input boundary of rectangle 1 and the output boundary of rectangle N respectively. Therefore, V_0 and V_{N+1} can be assigned to the applied port voltage sources.

Q_j is the total charge present on rectangle j and can be found by integrating the charge density over the volume of rectangle j .

$$Q_j = \int_{v_j} \rho dv_j \quad (2.25)$$

By solving equation (2.23) for ρ and inserting the result into equation (2.25), substituting the current \bar{J} with a summation of pulse basis functions, we get

$$Q_j = \frac{1}{j\omega} \int_{v_j} \sum_{i=1}^N \frac{(\nabla \bullet I_i \hat{J}_i) b(x, y, z)_i}{a_i} dv_j. \quad (2.26)$$

The divergence is taken on the volume current density in rectangle j . The result is a derivative with respect to the direction in which current is flowing. Again, a finite difference approximation can be made giving

$$Q_j = \frac{\Delta I_j}{j\omega} \quad (2.27)$$

Here ΔI_j is the difference between currents at the input and output boundaries of rectangle j . Current at the boundaries is assumed to be the average of the two rectangles sharing this boundary. Here we let $I_0 = I_1$ and $I_{N+1} = I_N$. By substituting (2.27) into (2.24), we obtain

$$V_i = \frac{1}{j\omega} \sum_{j=1}^N \frac{\Delta I_j}{v_i v_j} \int_{v_i} \int_{v_j} G_e dv_i dv_j. \quad (2.28)$$

Writing equation (2.28) in matrix form gives

$$[V] = \frac{1}{j\omega} [P][\Delta I]. \quad (2.29)$$

Here, $[P]$ is the well-known coefficient of potential matrix whose elements are

$$p_{ij} = \frac{1}{v_i v_j} \int_{v_i} \int_{v_j} G_e dv_j dv_i. \quad (2.30)$$

Calculate equation (2.30) using a discrete cosine transform, a technique outlined in [5] and [9] and summarized in Appendix B. Solving equation (2.29) for $[\Delta I]$ gives the matrix equation,

$$[\Delta I] = j\omega [P]^{-1} [V] = j\omega [C][V]. \quad (2.31)$$

2.4 Creating the Distributed Circuit from the System of Equations

Equations (2.22) and (2.31) are in the form of Kirchoff's voltage law (KVL) and Kirchoff's current law (KCL), respectively. From (2.31) we construct the circuit shown in Figure 5 using KCL with some algebraic manipulation as in [11]-[13] so that the topology of the circuit agrees with the properties of the capacitance matrix outlined in [14]. The capacitance of rectangle i to ground C_{ii} can be written as

$$C_{ii} = \sum_{j=1}^N c_{ij} \quad (2.32)$$

where c_{ij} are the individual terms of the $[C]$ matrix for an N rectangle system.

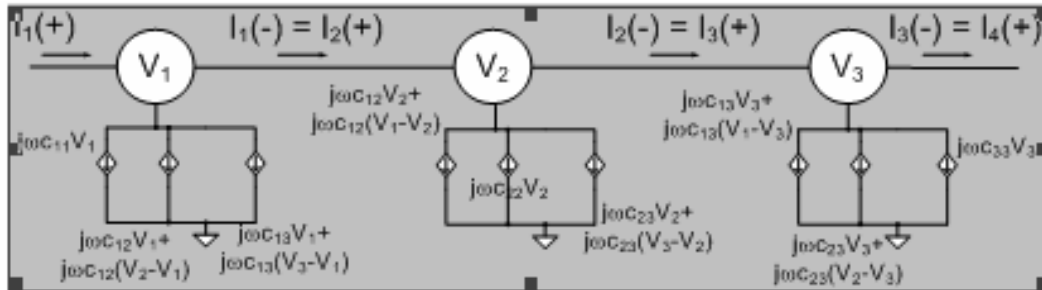


Figure 5 - Equivalent KCL for three series rectangles

Also, the direct capacitance between two rectangles i and j can be written as

$$C_{ij} = -c_{ij}. \quad (2.33)$$

This leads us to construct the circuit so that the current to ground from rectangle i is written as $j\omega C_{ii}V_i$ and the current from rectangle i to j is written as $j\omega C_{ij}(V_i - V_j)$. An equivalent circuit of Figure 5 is re-drawn with capacitors in Figure 6.

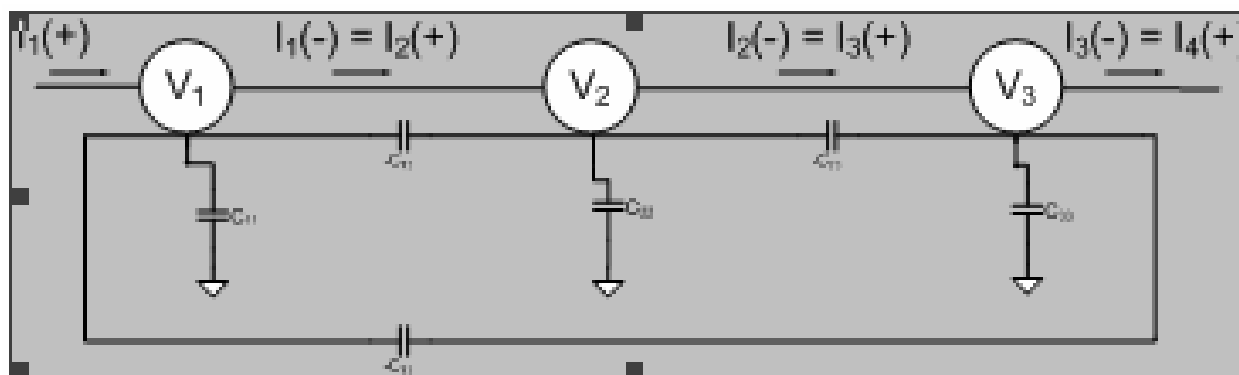


Figure 6 - Equivalent KCL with capacitors

To complete the derivation of the PEEC distributed circuit, we use equation (2.22) to model the ohmic loss and magnetic coupling within the metal of the inductor. Utilizing the KVL form of equation (2.22), the circuit in Figure 7 is developed.

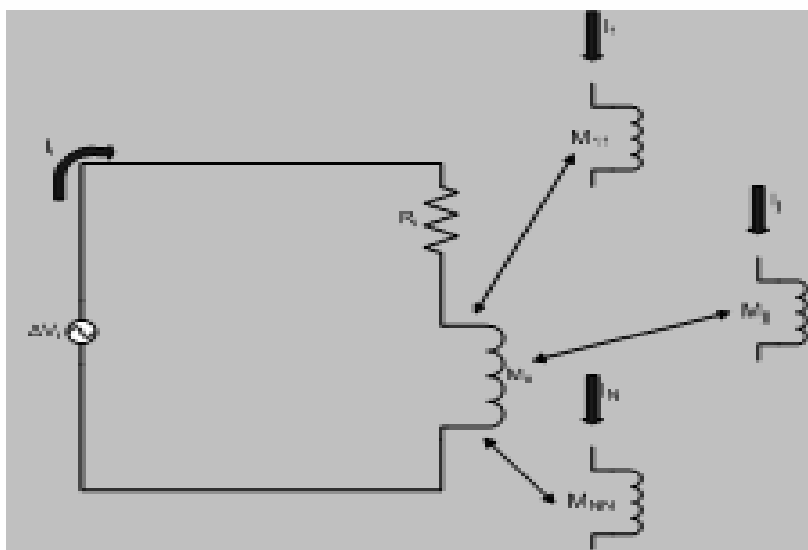


Figure 7 - KVL circuit for one rectangle

We combine the circuit of Figure 7, which represents the magnetic coupling and power loss in the conductor, with the circuit of Figure 6, which models the electrostatic coupling between different conductive segments and between the conductor and ground. The resulting distributed model is formed in Figure 8.

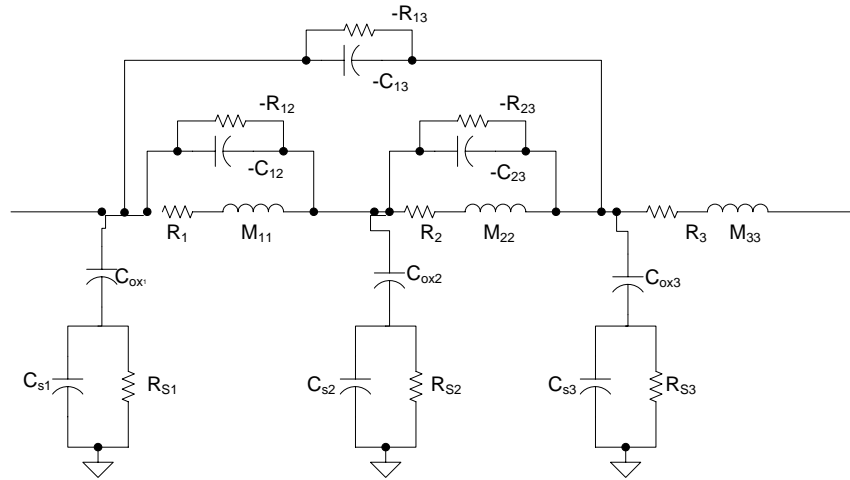


Figure 8 - PEEC distributed circuit for three series rectangles

The capacitors in Figure 4 are complex. This is related to the fact that G_e is complex and accounts for loss in the substrate. As a result, each partial capacitance is represented by an ideal capacitor in parallel with a resistor. The ideal capacitance is simply the real part of the partial capacitance. The parallel resistance is simply given by

$$R_{ij} = \frac{-1}{\omega(\text{imag}(C_{ij}))}. \quad (2.34)$$

From [5] we know that the imaginary part of C_{ij} is approximately inversely proportional to frequency, which tells us that R_{ij} is approximately constant with respect to frequency. The terms R_{ij} above are not to be confused with the terms of $[R]$, which is discussed in Chapter 3 and deals with the frequency dependent resistance.

The application of the distributed model to the inductor is simple. It is observed in Figure 3 that the rectangles comprising the inductor are in series from port 1 to port 2, allowing us to add the distributed models in series. Thus, for an inductor of twelve rectangles, we would have four of the circuits from Figure 8 in series.

Chapter 3 Calculating the Resistance Matrix

In Chapter 2, the current distribution is assumed to be uniform inside the volume of the rectangle. However, the current will be non-uniform due to the skin effect and, in the case of the spiral inductor, eddy currents. While a uniform current approximation is reasonably adequate for the calculation of the partial inductance and partial capacitance matrices, it is not adequate to calculate the resistance matrix.

3.1 Eddy Currents in a Spiral Inductor

We begin with a discussion of the derivation of $[R]$. The resistance matrix, $[R]$, is a diagonal matrix whose elements represent two important effects: the amount of power dissipated in each rectangle due to skin effect and eddy currents, as well as the effects due to the internal inductance of each rectangle. To calculate the total power dissipated in each rectangle, the total current in each rectangle is first calculated. As an approximation, the total current in a rectangle is expressed as a sum of an excitation current and an eddy current. The excitation current is uniform across the length and width of the rectangle. The eddy current describes how the current is disturbed by the presence of a magnetic field.

$$\bar{\mathbf{J}}_{tot} = \bar{\mathbf{J}}_{ex} + \bar{\mathbf{J}}_{eddy} \quad (3.1)$$

Applying equation (3.1) to the case of uniform excitation current and an eddy current density that is linear in x results in the illustration of Figure 9. The (+) sign indicates current is flowing into the paper and a (-) sign indicates current is flowing out of the paper.

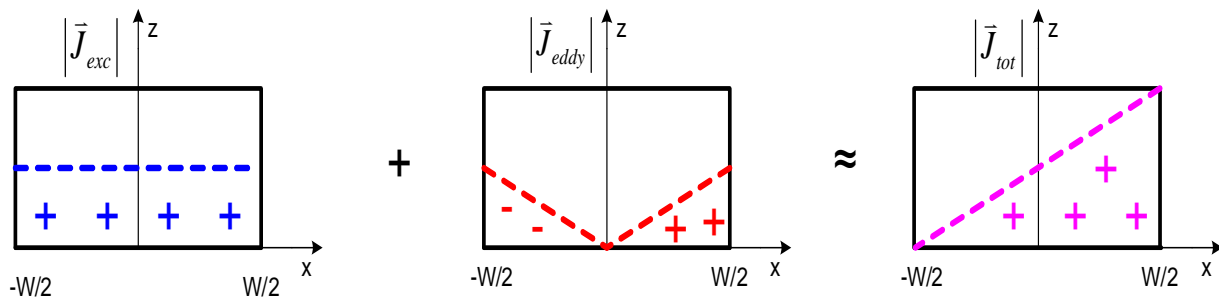


Figure 9 - Cross-section of a trace illustrating the total current distribution

The coordinate system for a rectangle is illustrated by Figure 10. The origin is located at the center of the rectangle.

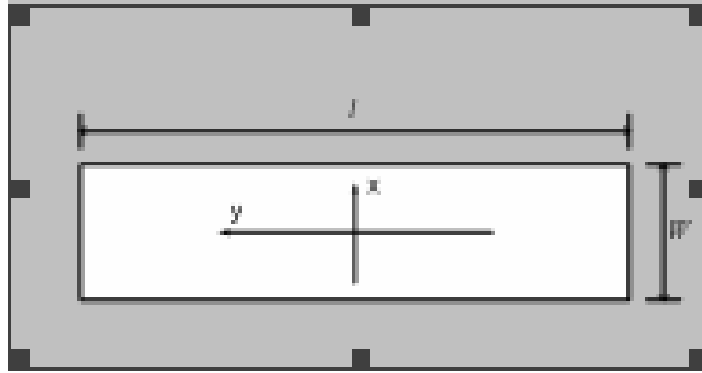


Figure 10 - Coordinate system for the top view of a rectangle

The author in [8] gives the relationship between eddy current density and the z-component of the magnetic flux, using Maxwell's equations, as

$$\bar{J}_{eddy} = \sigma \bar{E}_y = j\omega\sigma \hat{y} \int_0^x B_z(x') dx' \quad (3.2)$$

Note that the x-component of the eddy current is neglected since the length of the rectangle is assumed to be much larger than the width. A reasonable approximation in (3.2) is to assume that B_z is constant, then \bar{J}_{eddy} is linear in x . A more accurate formulation would be to allow \bar{J}_{eddy} to vary as x^α , where α is a constant, determined empirically, that is dependent on the technology being used. This allows equation (3.2) to be re-written in a more general form as

$$\bar{J}_{eddy} = j\omega\sigma B_z x^\alpha \hat{y}. \quad (3.3)$$

The author in [8] uses an empirical approximation for B_z . However, the magnetic flux acting on a given rectangle can be approximated using the partial inductance matrix found from equation (2.18). The total flux acting on rectangle i is

$$\psi_i = \sum_{j=1}^N M_{ij} I_j. \quad (3.4)$$

By assuming uniform flux distribution over the area of rectangle i , the magnitude of the magnetic flux density can be approximated as

$$B_{zi} \approx \frac{\sum_{j=1}^N M_{ij} I_j}{W_i l_i}. \quad (3.5)$$

The components of the partial inductance matrix that will contribute to the \hat{z} component of B , M_{zi} , can be determined by the right hand rule. Orthogonal rectangles have zero mutual inductance. We neglect the self-inductance term, because the magnetic field generated by rectangle i will have a zero average z component inside its volume. From [11], a general expression for M_{zi} is given as

$$M_{zi} = \sum_{n=1, n \neq i}^N (-1)^{\alpha_{in}} M_{in}, \quad (3.6)$$

where α_{in} is determined by the orientation of rectangle i relative to rectangle n and is equal to zero or one. Our expression for B_z on rectangle i is

$$B_{zi} = \frac{M_{zi} I_{ex}}{W_i l_i}. \quad (3.7)$$

3.2 The Skin Effect

In general, a conductor with a rectangular cross section will have current crowding at all of the surfaces as illustrated by Figure 11. The current crowding at high frequencies is due to the internal inductance being higher in the center of the conductor as a result of the internal magnetic field being largest at the center. The current tends to flow through the path of least impedance, which is the path of least inductance at high frequencies.



Figure 11 - Cross-section of current distribution

An exact calculation, in terms of number of skin depths Δ ($1 \leq \Delta \leq 2$) of the thickness that the current in the conductor penetrates is not a trivial task and its result will vary from technology to technology, depending greatly on the dielectric properties of the multilayer substrate being used. Using Δ as a variable for the number of skin depths the current takes up, the volume current density in the rectangle can be expressed as

$$\bar{J}(x, y, z) = \Delta * J(x, y) e^{\frac{z_i - z}{\delta}} \hat{y}. \quad (3.8)$$

Here, z_i , is the distance from the top of the substrate to rectangle i . z is equal to zero at the top of the substrate and is negative inside the substrate. Integrating equation (3.8) over the thickness of the conductor gives

$$\int_{-z_i}^{t-z_i} \bar{J}(x, y, z) dz = \Delta * \hat{y} J(x, y) \left(\delta - \delta e^{\frac{-t}{\delta}} \right). \quad (3.9)$$

The effective thickness, t_{eff} , is then defined as

$$t_{eff} = \Delta * \delta \left(1 - e^{\frac{-t}{\delta}} \right). \quad (3.10)$$

As we will see, t_{eff} plays a critical role in determining the frequency dependent resistance and therefore the peak Q of the device. This allows Δ to be treated as a degree of freedom that will be determined empirically for each technology. Using Q obtained by another EM solver or from measured data as a benchmark, Δ is adjusted so that the peak Q obtained by this model matches that of the EM solver or measured data. For the technology used in this model, a value of $\Delta = 1.1$ is used.

3.3 Calculating the Frequency Dependent Resistance

The total power dissipated in the rectangle can be expressed in terms of the total volume current density in the rectangle.

$$P_{diss} = \int_v \frac{1}{2\sigma} |\bar{J}_{tot}|^2 dv \quad (3.11)$$

We first substitute equation (3.7) into equation (3.3) for B_z , plugging that result into equation (3.1) and equation (3.11). Equation (3.11) is then integrated which gives the total power dissipated as

$$P_{diss} = \frac{t_{eff} l_i}{2\sigma} |J_{ex}|^2 \left\{ W_i + \frac{K}{2\alpha + 1} \left[\left(\frac{W_i}{2} \right)^{2\alpha + 1} - \left(-\frac{W_i}{2} \right)^{2\alpha + 1} \right] \right\}. \quad (3.12)$$

The variable K is defined as

$$K = \left(\frac{\omega \sigma M_{zi} t_{eff}}{l_i} \right)^2. \quad (3.13)$$

The effective resistance of the rectangle relates the amount of power dissipated in the rectangle to the amount of current applied to the rectangle.

$$R_{eff} = \frac{2P_{diss}}{|I_{ex}|^2} = \frac{2P_{diss}}{\left| \int_{S_{cross}} (\bar{J}_{ex} \bullet d\bar{S}_{cross}) \right|^2} \quad (3.14)$$

Evaluating the integral gives

$$\int_{-z_i}^{t-z_i} \int_{-\frac{W}{2}}^{\frac{W}{2}} \bar{J}_{ex} \bullet \hat{y} dx dz = J_{ex} W t_{eff} \quad (3.15)$$

The result of equation (3.15) and equation (3.12) is then combined into equation (3.14), which results in $R_{eff,ind}$ for a given rectangle i of an inductor being

$$R_{eff,ind} = \frac{l_i}{\sigma W_i^2 t_{eff}} \left\{ W_i + \frac{K}{2\alpha + 1} \left[\left(\frac{W_i}{2} \right)^{2\alpha+1} - \left(-\frac{W_i}{2} \right)^{2\alpha+1} \right] \right\}. \quad (3.16)$$

As with t_{eff} , α is also determined empirically by the comparison of Q between this model and another reliable benchmark. The procedure for determining α is to start off with $\alpha = 1$. The value for t_{eff} is varied first, as its value will affect Q the most. The value for t_{eff} will always be between one and two. If adjusting t_{eff} does not give a correct value for peak Q , t_{eff} will be set to the value that gives the best Q . Next, the value for α , is adjusted. Its value should not be too far from 1, as the linear approximation for the eddy current distribution is fairly accurate. For this model, the linear approximation for the eddy current distribution, $\alpha = 1$, is used.

The rectangles of the inductor will experience an internal inductance because of the magnetic flux internal to the conductor. Paul [3] gives the per-unit-length internal inductance of a circular wire as

$$L^{int} = \frac{2\delta}{r_w} \left(\frac{\mu_o}{8\pi} \right) \quad (3.17)$$

for high frequencies ($r_w \gg \delta$) and

$$L^{int} = \frac{\mu_o}{8\pi} \quad (3.18)$$

for low frequencies ($r_w \ll \delta$). Here, r_w is the radius of the wire. 2δ is recognized as the effective thickness of the wire. As the conductor is rectangular, it is unknown what should be substituted into r_w . However, if we assume that at DC, the per-unit-length internal inductance should be

equation (3.18), then it is reasonable to approximate the per-unit-length internal inductance for all frequencies as

$$L^{\text{int}} = \frac{t_{\text{eff}}}{t} \left(\frac{\mu_0}{8\pi} \right), \quad (3.19)$$

because at low frequencies, t_{eff} is approximately equal to t . The total reactance of the rectangle can be calculated as

$$X_{\text{eff}} = \omega L^{\text{int}} l. \quad (3.20)$$

Chapter 4 Deriving the Inductor Lumped Pi-Model

The techniques of Chapters 2 can be used to construct a PEEC distributed model for any planar monolithic inductor. Shown in Figure 12 is a flowchart outlining the progression from Maxwell's equations to an inductor lumped pi-model.

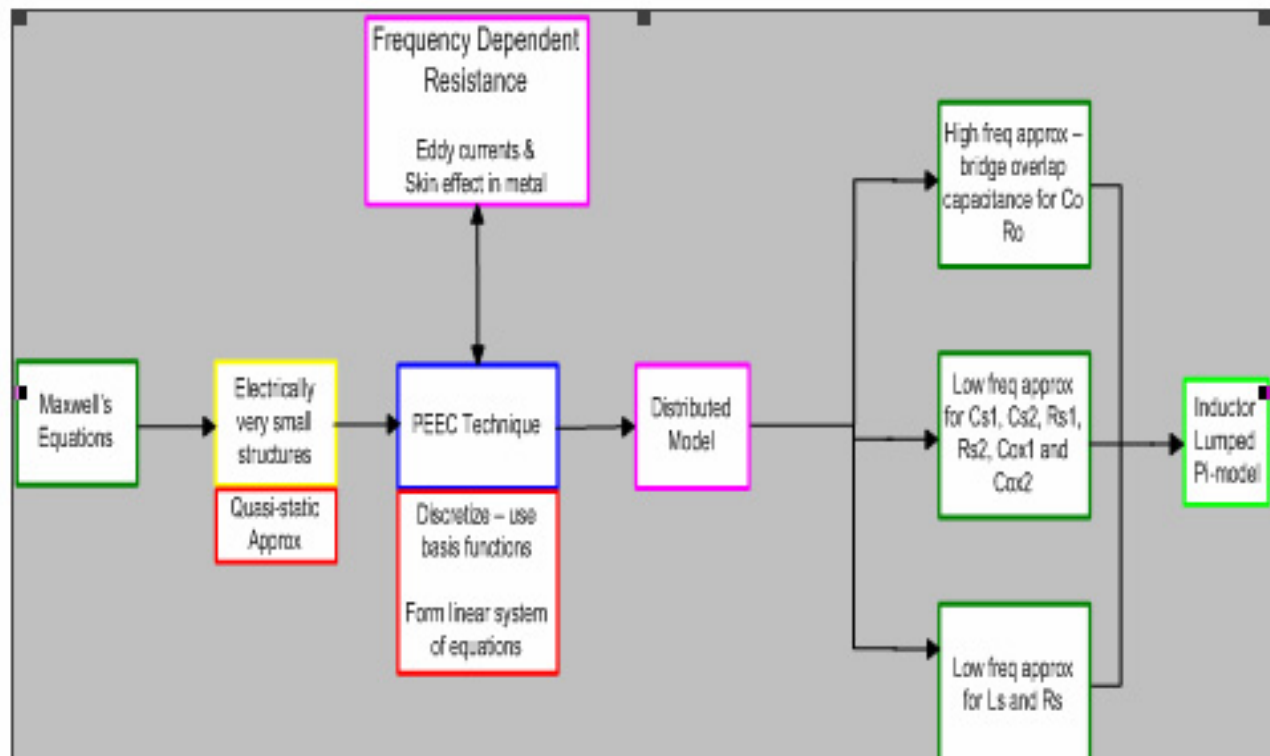


Figure 12 - Inductor lumped pi-model derivation flowchart

In this chapter, we describe a method to simplify the distributed model down to a lumped pi-model for a spiral inductor. A lumped pi-model makes it easy for the designer to visualize the parasitics inherent to the spiral inductor. The inductor lumped pi-model we use is commonly used for integrated inductors and is shown in Figure 13. The loss in the substrate due to the electrostatic coupling between metal and ground is captured by R_{s1} and R_{s2} . The capacitance caused by this electrostatic coupling through the substrate is captured by C_{s1} and C_{s2} . The capacitive coupling due to the lossless oxide is represented by C_{ox1} and C_{ox2} . The lumped model used by [11]-[13] does not account for this oxide capacitance separately from C_{s1} , R_{s1} , C_{s2} , and R_{s2} . By taking into account the effect due to C_{ox1} and C_{ox2} separately from the rest of the substrate admittance, we are able to accurately model the device at lower frequencies. If C_{ox1} and C_{ox2} are absent, we effectively have a low impedance to ground through R_{s1} and R_{s2} at low frequencies, which is physically not accurate since the lossless oxide would make the impedance very large.

As mentioned in Chapter 1, there are approximate empirical and semi-analytical methods ([1], [6], [8], [15], [16]) used to calculate the component values of the lumped pi-model. As illustrated in the flowchart in Figure 12, we use two low frequency approximations to the distributed model similar to that of [11]-[13] to calculate R_s , L , $C_{s1,2}$ and $R_{s1,2}$. We use a high frequency approximation that uses the overlap capacitance of the inductor bridge to approximate a value for C_0 and R_0 .

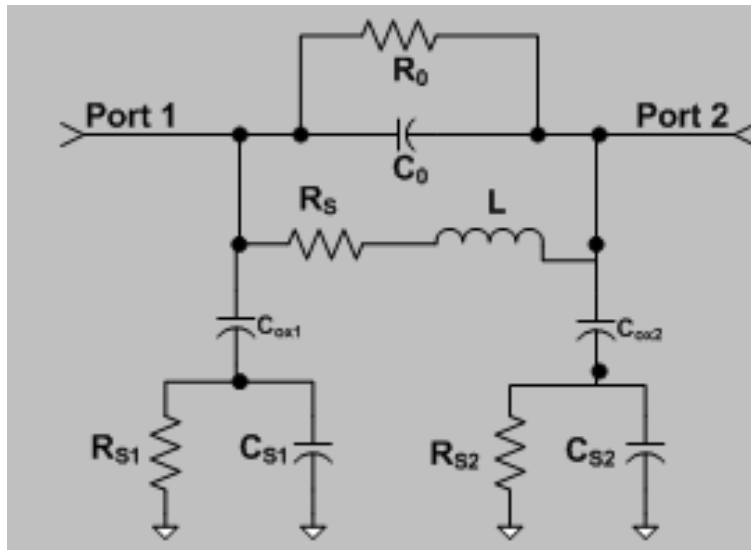


Figure 13 - Inductor lumped pi-model

4.1 First Low Frequency Approximation

The first low frequency approximation involves recognizing that at low frequencies, the complex capacitors are approximately open circuits. By applying this approximation to the PEEC circuit of Figure 8, the circuit of Figure 14 results.

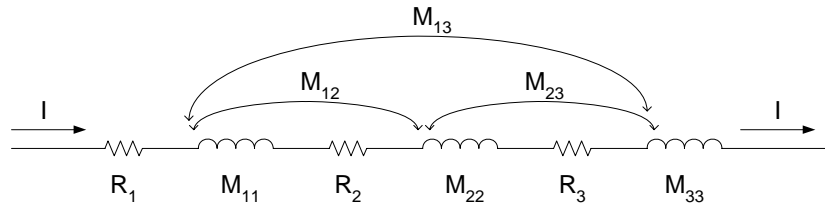


Figure 14 - Distributed circuit following a low frequency approximation

For a circuit with N series rectangles, it is easily observed that the total series impedance of this circuit is

$$Z_{series} = \sum_{i=1}^N R_i + s \sum_{i=1}^N \sum_{j=1}^N M_{ij} \quad (4.1)$$

The form of equation (4.1) is

$$Z_{series} = R_s + sL \quad (4.2)$$

which is the same form as the branch of the pi-model shown in Figure 15.

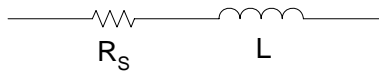


Figure 15 - Pi-circuit neglecting capacitances

Thus the components of Figure 14 can be found as

$$R_s = \sum_{i=1}^N R_i \quad (4.3)$$

$$L = \sum_{i=1}^N \sum_{j=1}^N M_{ij} \quad (4.4)$$

4.2 Second Low Frequency Approximation

The second low frequency approximation does not neglect all of the capacitors. Because the impedance of an inductor is much smaller than the impedance of a capacitor at low frequencies, the complex capacitances in parallel with a series RL combination are neglected. All of the complex capacitances connected to ground remain. When this approximation is applied to the PEEC circuit of Figure 8, the result is the circuit of Figure 16. The currents through each of the rectangles of the inductor are assumed to be approximately equal because of the negligible current in the substrate. This allows us to lump the mutual inductances with the self-inductances.

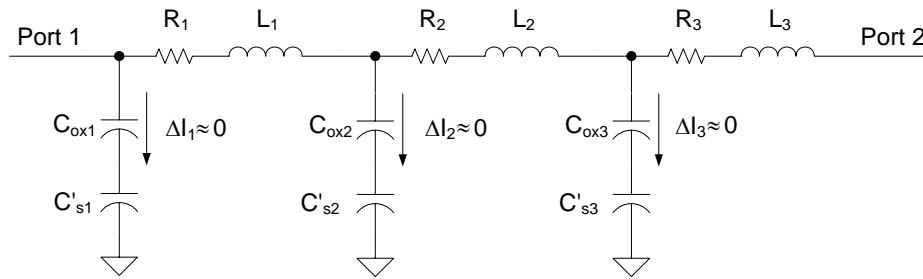


Figure 16 - PEEC circuit after second low frequency approximation

$$L_i = \sum_{j=1}^N M_{ij} \quad (4.5)$$

The next step is to short port 2 and calculate the input admittance Y_{11} . We ignore terms with s to the power of three or greater since we are using a low frequency approximation. This gives

$$Y_{11} \approx s \left(\frac{C_{ox1} C'_{s1}}{C_{ox1} + C'_{s1}} + \alpha_2 \frac{C_{ox2} C'_{s2}}{C_{ox2} + C'_{s2}} + \alpha_3 \frac{C_{ox3} C'_{s3}}{C_{ox3} + C'_{s3}} \right) + \frac{1}{Z_{series}} \quad (4.6)$$

where Z_{series} is found from equation (4.1) and

$$\alpha_i = \frac{s \sum_{j=i}^N L_j}{Z_{series}} \approx \frac{s \sum_{j=i}^N L_j}{L} \quad (4.7)$$

if we assume $sL_i \gg R_i$ as in [11] to make the substrate impedance independent of frequency. The form of equation (4.6) matches the form for the input admittance looking into the circuit of Figure 17.

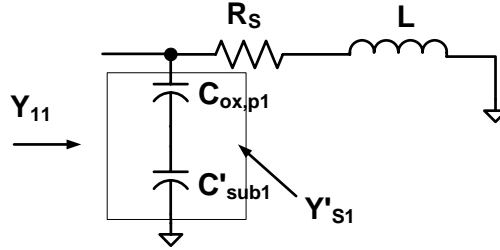


Figure 17 - Low frequency pi-circuit with port 2 shorted

$$Y_{11} = sY'_{s1} + \frac{1}{R_s + sL} \quad (4.8)$$

Equating equation (4.6) to equation (4.8) for N rectangles gives the substrate admittance Y'_{s1} . Since $s=j\omega$ and keeping in mind that C'_{si} is complex,

$$\begin{aligned} Y'_{s1} &= \sum_{i=1}^N \alpha_i Y'_{si} = \sum_{i=1}^N \alpha_i \frac{C_{oxi} C'_{si}}{C_{oxi} + C'_{si}} = j\omega \left\{ \text{Re}(\tilde{Y}'_{s1}) \right\} + j\omega \left\{ j * \text{Im}(\tilde{Y}'_{s1}) \right\} \\ &= j\omega \left\{ \text{Re}(\tilde{Y}'_{s1}) \right\} - \omega \left\{ \text{Im}(\tilde{Y}'_{s1}) \right\} \end{aligned} \quad (4.9)$$

where Y'_{s1} is the total complex admittance to ground at port 1 as illustrated in Figure 17. Y'_{si} is the total complex capacitance to ground of rectangle i and is found from the capacitance matrix as

$$Y'_{si} = \sum_{j=1}^N c_{ij}, \quad (4.10)$$

where c_{ij} represents the individual terms of $[C]$.

In a manner similar to [15] and [16], we use a parallel plate approximation for the oxide capacitance. This gives the oxide capacitance in terms of the area, thickness, and permittivity of rectangle i as

$$C_{oxi} = A_i \frac{\epsilon_{ox}}{t_{ox}}, \quad (4.11)$$

where A_i is the surface area (neglecting thickness) of rectangle i . We make the assumption that the oxide capacitance is equal at both ports; therefore, we can take the sum of the oxide capacitance due to all the rectangles and divide it by two to calculate the oxide capacitance at port 1 and port 2.

$$C_{ox,p1} = C_{ox,p2} = \frac{1}{2} \sum_{i=1}^N C_{oxi} \quad (4.12)$$

We can express Y'_{s1} as the series combination of the admittances due to C'_{sub1} and $C_{ox,p1}$, which are defined in Figure 17.

$$Y'_{s1} = j\omega \left\{ \frac{C_{ox,p1} C_{R,1} (C_{R,1} + C_{ox1}) + C_{ox,p1} C_{I,1}^2}{(C_{R,1} + C_{ox,p1})^2 + C_{I,1}^2} \right\} - \omega \left\{ \frac{C_{ox,p1}^2 C_{I,1}}{(C_{R,1} + C_{ox,p1})^2 + C_{I,1}^2} \right\} \quad (4.13)$$

where $C_{I,1} = \text{Im}\{C'_{sub1}\}$ and $C_{R,1} = \text{Re}\{C'_{sub1}\}$. Equating the real and imaginary parts of equation (4.9) with the real and imaginary parts of equation (4.13) gives us two equations to solve for the two unknowns, $C_{I,1}$ and $C_{R,1}$. From $C_{I,1}$ and $C_{R,1}$ we use the complex capacitance technique to extract the component values, C_{sub1} and R_{sub1} .

$$C_{sub1} = C_{R,1} \quad (4.14)$$

$$R_{sub1} = -\frac{1}{\omega C_{I,1}} \quad (4.15)$$

This technique will work for any $\omega > 0$. A similar procedure is applied to find the component values at port 2.

$$\begin{aligned} Y'_{s2} &= \sum_{i=1}^N \beta_i Y'_{si} = \sum_{i=1}^N \beta_i \frac{C_{oxi} C'_{si}}{C_{oxi} + C'_{si}} = j\omega \left\{ \text{Re}(\tilde{Y}'_{s2}) \right\} + j\omega \left\{ j * \text{Im}(\tilde{Y}'_{s2}) \right\} \\ &= j\omega \left\{ \text{Re}(\tilde{Y}'_{s2}) \right\} - \omega \left\{ \text{Im}(\tilde{Y}'_{s2}) \right\} \end{aligned} \quad (4.16)$$

$$\beta_i = \frac{\sum_{j=1}^i L_j}{L} \quad (4.17)$$

$$C_{sub2} = C_{R,2} \quad (4.18)$$

$$R_{sub2} = -\frac{1}{\omega C_{I,2}} \quad (4.19)$$

4.3 High Frequency Approximation

For an accurate calculation of the self-resonant frequency, the most important component of the equivalent pi-model apart from the inductance is the interwinding capacitance C'_0 , the parallel combination of R_0 and C_0 in Figure 13. While the frequency dependent resistance plays an important role in determining the value of the peak Q of the inductor, the interwinding

capacitance determines when the inductor Q becomes zero and the inductor behaves as a capacitor rather than an inductor. We replace the complete distributed model for three consecutive rectangles with the simplified version shown in Figure 18 for 4 rectangles, where the inductors are treated as open circuits. Note we also replace the admittances to ground from each rectangle with the lumped values at the ports found with the second low frequency approximation.

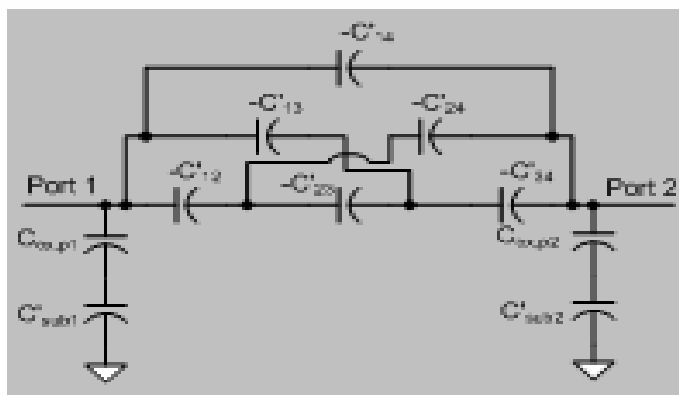


Figure 18 - High frequency approximation for four series rectangles

Our method is based on a common technique used in other analytical pi-models, such as [15] and [16], which use the overlap capacitance of the bridge, illustrated in Figure 19, to determine the interwinding capacitance.

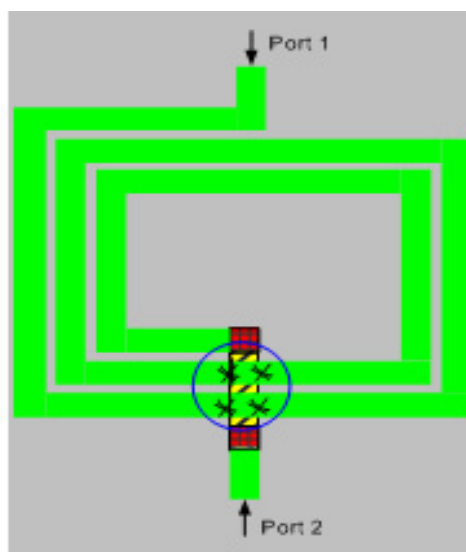


Figure 19 - Illustration of bridge overlap capacitance – 2.5 turn inductor

The methods in [15] and [16] use a parallel plate approximation, whereas we use the $[C]$ matrix, which is more accurate in that it accounts for fringing. In order to justify the method of using the overlap capacitance to determine the total interwinding capacitance, we must show that the portion of the inductor that overlaps the bridge is close to the port 1 voltage and that the bridge is close to the port 2 voltage at resonance. Once this is accomplished, we can ignore all of the turn-to-turn interwinding capacitances because most of the turns are at the same potential and the overlap capacitance will dominate. After inspecting the voltage along the inductor for various geometries by solving the above equations, we consistently find that the voltage along the first half of the inductor rectangles remained fairly constant and that most of the voltage drop occurred along the inner-most turns of the inductor after the last overlap of the bridge. The plot of the voltage along the inductor at resonance is shown below for a 1.5 turn and 3.5 turn inductor in Figure 20 and Figure 21, respectively, and it shows that the overlap rectangles are close to the same voltage as port 1. Similar results were found for other N-turn inductors.

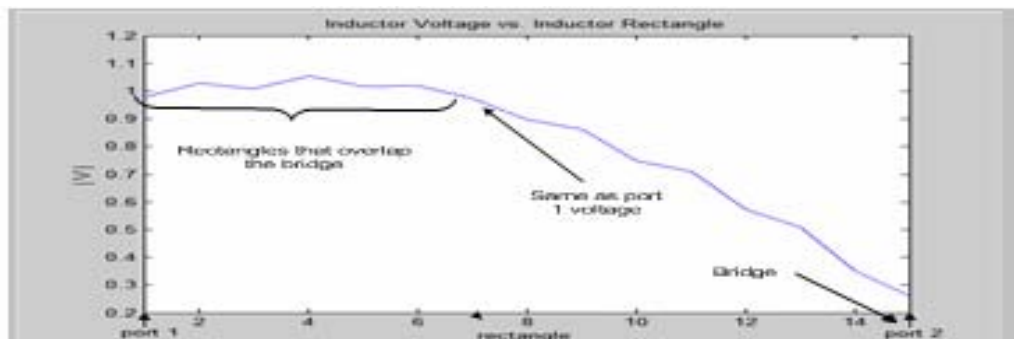


Figure 20 - Inductor voltage vs. Inductor rectangle for 1.5 turn inductor

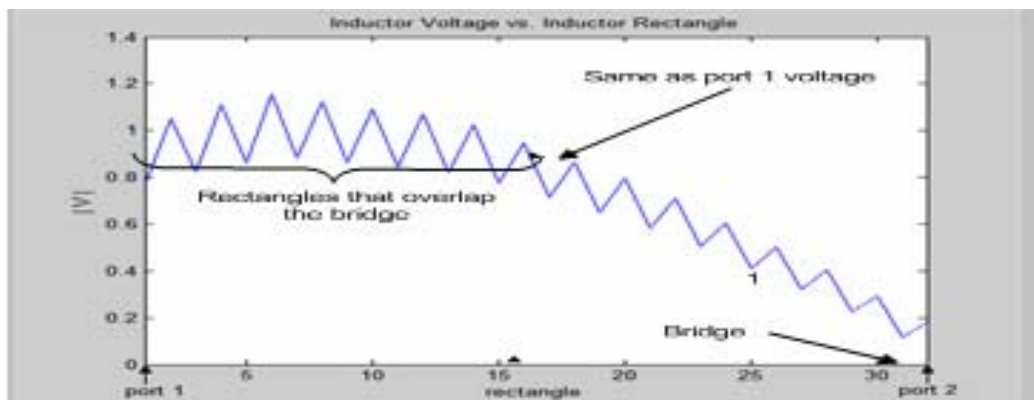


Figure 21 - Inductor voltage vs. Inductor rectangle for 3.5 turn inductor

As a result of these findings, we can express the total interwinding capacitance as the parallel combination of each bridge overlap capacitance. A general expression for the discretization scheme shown in Figure 3 and used in this model is given as

$$C'_0 = \sum_{\substack{i=6 \\ \text{step } 8}}^{\gamma-9} \{c(i, \gamma) + c(i+1, \gamma)\} \quad (4.20)$$

$$\gamma = 8N + 3 \quad (4.21)$$

$$c(i, j) = -C(i, j) \quad (4.22)$$

with N being the number of turns of the inductor.

We use the complex capacitance technique to extract the real capacitance and resistance values from the complex capacitance.

$$C_0 = \text{real}(C'_0) \quad (4.23)$$

$$R_0 = -\frac{1}{\omega(\text{imag}(C'_0))} \quad (4.24)$$

Chapter 5 Comparison with Momentum and Measured Data

5.1 Inductor Results

A set of five spiral inductors was designed, with the 1.5 turn design being done by Idstein [11], with turns varying from 1.5 to 5.5 turns as described by Table 1. The substrate used is based on a 0.18 μm FDSOI CMOS technology, a process utilizing a high resistivity (2000 $\Omega\text{-cm.}$) bulk silicon substrate. A description of the layer stack and its properties is given in Tables 2 and 3.

Table 1 - Inductor geometry summary

Inductor #	Inductance (nH)	Number of turns	Outer diameter (μm)	Trace width (μm)	Trace spacing (μm)
1	1	1.5	248	28	4
2	2.5	2.5	248	14	4
3	1.6	3.5	146	10	4
4	3	4.5	190	10	5
5	4.9	5.5	210	10	4

Material	Thickness (um)	Dielectric Constant	Conductivity (S/m)
Oxide	7.75	4	0
Silicon	675	11.7	0.5

Table 2 - Substrate dielectric properties

Metal Layer	Thickness (um)	Distance from metal center to top(um)	Conductivity (S/m)
Metal 1	.6	6.15	2.08E+07
Metal 2	.6	4.55	2.08E+07
Metal 3	2	1.75	2.64E+07

Table 3 - Substrate metal properties

Using the concepts discussed in this report, the component values of the lumped pi-circuit of Figure 13 were calculated. The lumped pi-circuit was then simulated using the Agilent ADS schematic tool. The ADS schematic showing the pi-circuit and its component values for inductor #1 is given in Figure 22. The box in the middle of the schematic titled “SNP1” contain the 2-port S-parameters of the frequency dependent impedance. The 2-port S-Parameters were computed from 100 MHz to the first resonant frequency of each inductor. The inductors were also simulated using ADS RF Momentum, which is a Method of Moments (MoM) EM simulator. Measured data was obtained for inductor #1, the 1.5 turn spiral. The layout of the test structure is illustrated by Figure 23. The pads are arranged in a ground-signal-ground configuration and 2-port S-Parameter measurements from 1-20 GHz were performed using on-chip cascade probes.

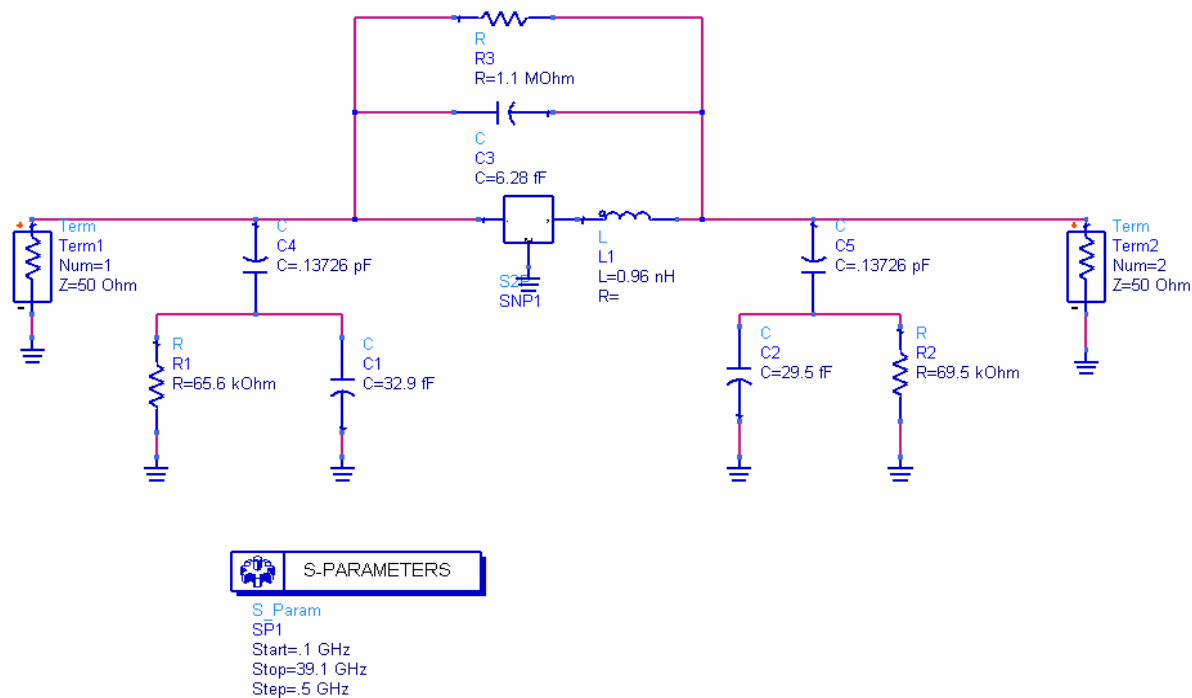


Figure 22 - ADS schematic for inductor #1

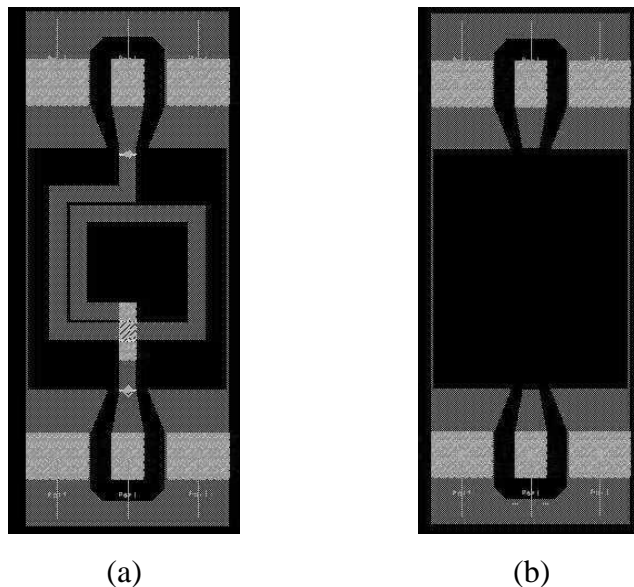


Figure 23 - 1.5 turn inductor (a) and open (b) test structure

The measured data was de-embedded by subtracting the Y-Parameters ($Y_{11} + Y_{12}$, $Y_{22} + Y_{12}$) of the de-embed open (Figure 23b) from the measured Y-Parameters. This effectively

removes the parasitic pad capacitance from the measurements. For the other inductors, the 2-port S-Parameters generated from the Momentum simulation were used as the benchmark to compare our model to.

The differential impedance, which describes the series impedance connecting ports 1 and 2, is defined using the Z-Parameters of the 2-port inductor.

$$Z_{diff} = Z_{11} + Z_{22} - Z_{12} - Z_{21} \quad (5.1)$$

Using the differential impedance, the effective inductance of the inductor can be computed at frequency f as

$$L_{eff} = \frac{\text{imag}(Z_{diff})}{2\pi f}. \quad (5.2)$$

The inductor Q can also be computed using the differential impedance as

$$Q = \frac{\text{imag}(Z_{diff})}{\text{real}(Z_{diff})}. \quad (5.3)$$

The values for Q and L_{eff} , as well as the 2-port S-Parameters generated by Momentum and our model were then compared. Again, we were able to compare to measured data for inductor #1. As can be seen from Figure 24 – Figure 28, reasonable agreement between Momentum and our model is achieved. Additionally, our model agrees well with the de-embedded measured data in predicting the frequency and value of the peak Q , as well as accurately modeling effective inductance and S-parameters, as can be seen in Figure 29.

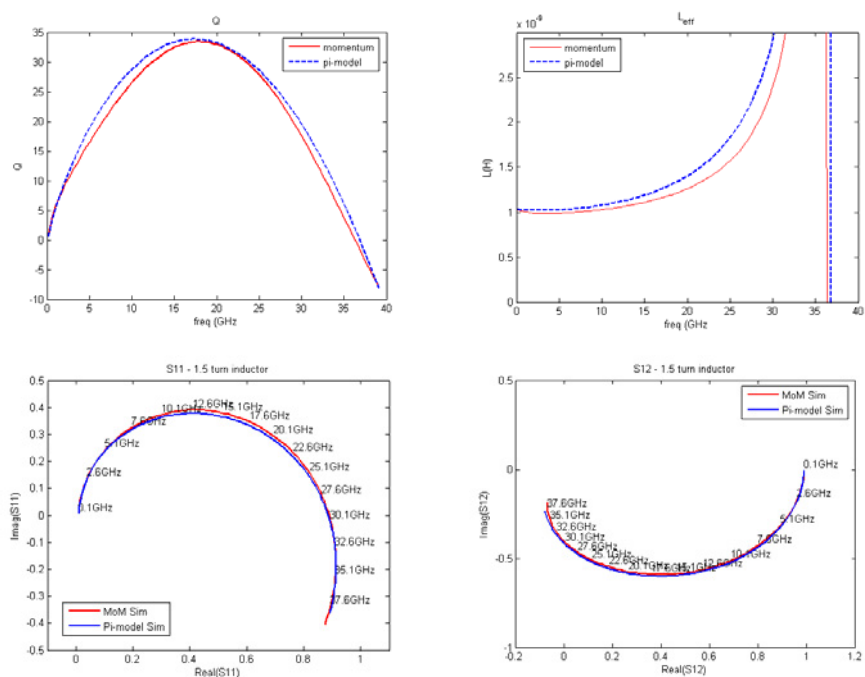


Figure 24 - Simulated results inductor #1

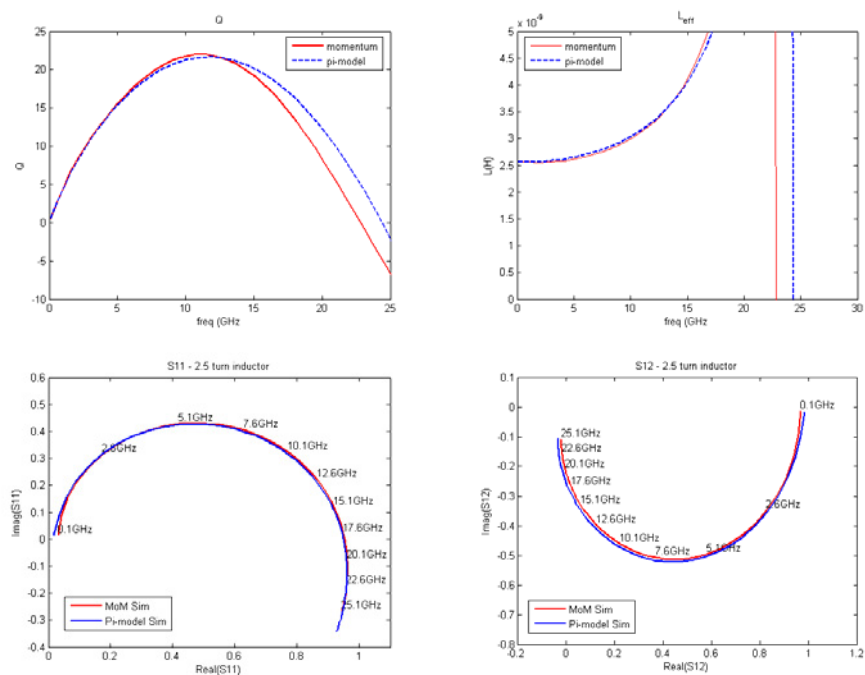


Figure 25 - Simulated results inductor #2

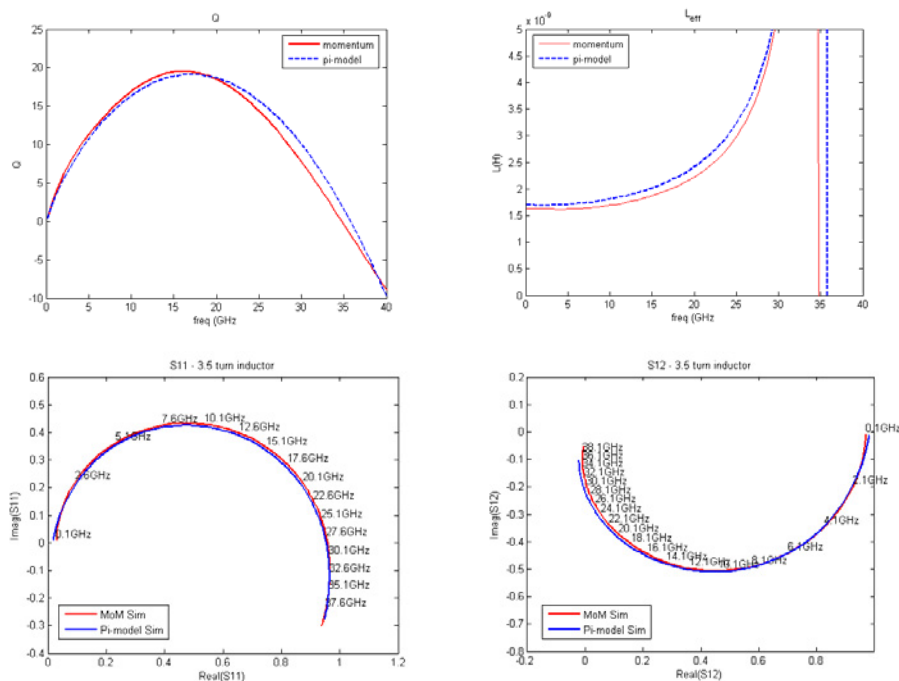


Figure 26 - Simulated results inductor #3

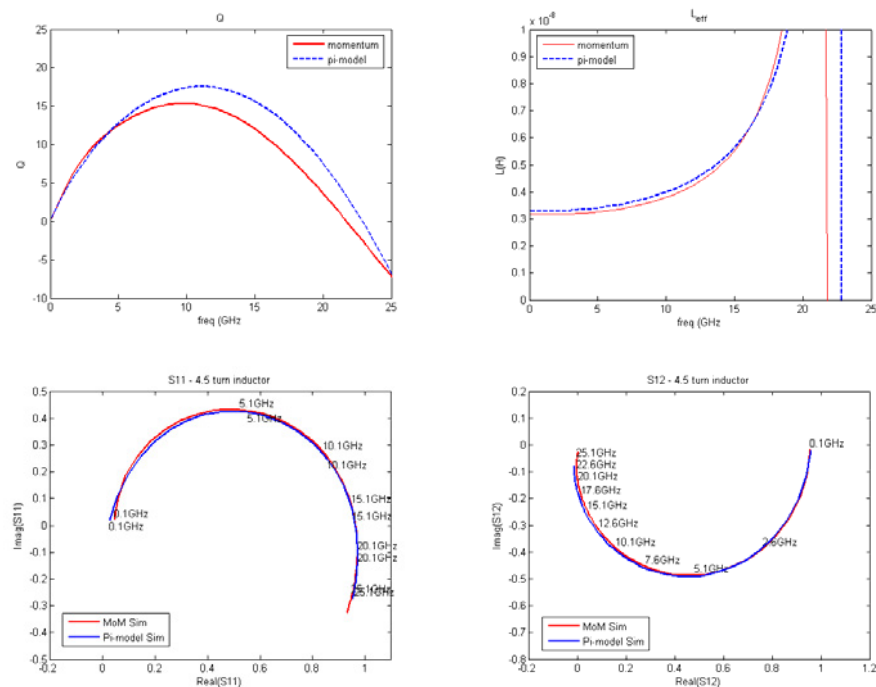


Figure 27 - Simulated results inductor #4

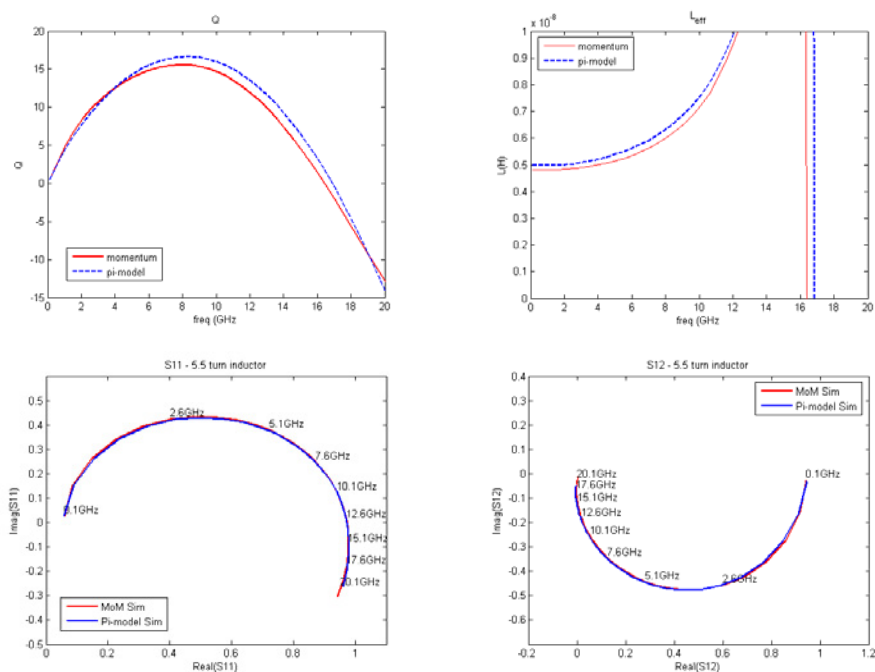


Figure 28 - Simulated results inductor #5

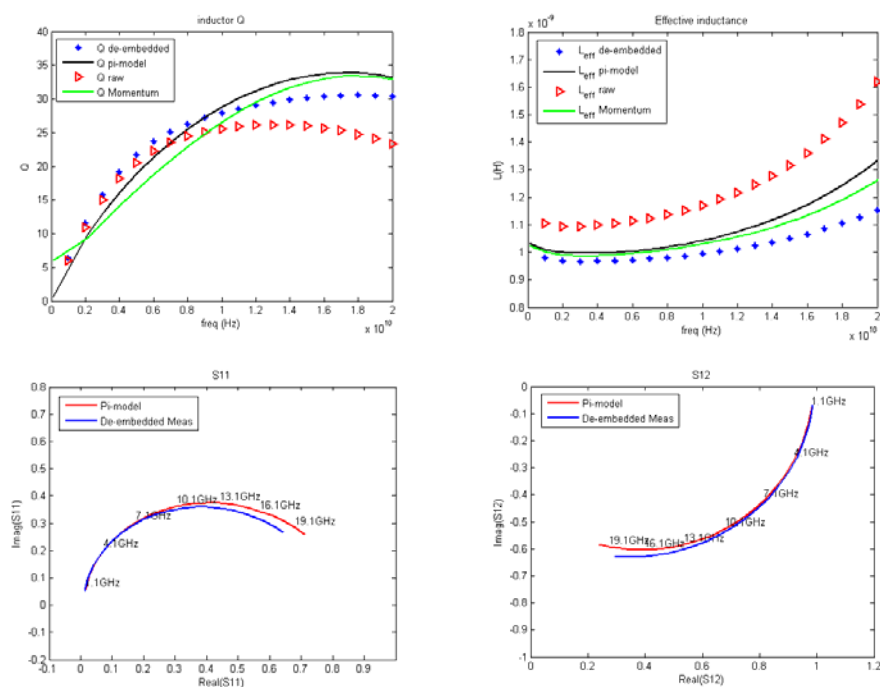


Figure 29 - De-embedded measured results for inductor #1

The biggest discrepancy observed is in the prediction of Q at higher frequencies. It is typical for Q to vary slightly from one model to the next, as the methods of capturing the ohmic loss in the metal are usually different. The most important aspect of Q is the magnitude and frequency of its maximum, since this is typically in the frequency range that the device will be used. In comparing our model with Momentum, the peak Q is reasonably close, and the peak Q frequencies are nearly identical which leads to a high degree of confidence in both models. Slight deviations in the effective inductance values are most likely due to approximations made in the modeling of internal inductance. The slight over-estimation in the resonant frequency is most likely due to the method in determining the interwinding capacitance, which neglects some of the turn-to-turn capacitances and relies only on the bridge overlap capacitance for its value.

Chapter 6 Summary and Conclusions

In this report, the technique proposed in [11]-[13] for modeling spiral inductors with a simple lumped pi-circuit was improved upon. In addition, the bandwidth of this model goes up to the first resonant frequency, a significant improvement in the bandwidth achieved previously.

As in [11]-[13], the PEEC technique was used to construct the distributed circuit, upon which the lumped pi-circuits were based. A low frequency approximation similar to that in [11]-[13] was applied to the distributed circuit to arrive at values for the substrate impedance and series impedance of the inductor. The method in this work differs slightly in that it accounts for the lossless oxide capacitance. At higher frequencies, a different method was used to determine the interwinding capacitance. This method has also been used in [15] and [16], but we justify its application by inspecting the voltage along the inductor near resonance. As previously mentioned, the interwinding capacitance must be calculated accurately in order to correctly predict the resonant frequency.

In calculating the partial capacitance matrix, [11]-[13] used numerical integration which proved to be very time-consuming. A method employing FFTs as discussed by [5] was used in this work to speed up the calculation of $[C]$.

As demonstrated in Chapter 5, good agreement in Q , L_{eff} , and 2-port S-parameters up to the first resonance is obtained with the inductor model presented in this work and ADS RF Momentum. We also verify the accuracy of the model by comparing to the de-embedded measurements for a 1.5 turn 1 nH inductor.

A big improvement that could be made to this model would be to account for eddy current losses in the substrate when calculating the partial inductance matrix $[M]$. To accomplish this, a multi-layer G_m would need to be calculated, as mentioned in Chapter 2. The technique outlined in [19], using image theory, could be used as a guideline for calculating G_m . One potential problem with using a G_m that accounts for loss is that the matrix $[M]$ will become frequency dependent, which leads to a somewhat more complicated model.

Another improvement to the inductor model would be to allow for more general geometries, such as octagonal spirals or circular spirals. As the shape of a spiral inductor approaches circular, the efficiency in terms of inductance per-unit-area increases, leading to more efficient use of real-estate in the integrated circuit design. The only change that needs to be done is to modify the existing computer program (MATLAB).

The model discussed in this report is based on rigorously derived equations that are true to the physics of the device. The S-parameter data generated in the ADS schematic can be incorporated into other circuit simulators such as Cadence and used in the design of complex integrated circuits such as LNAs, matching networks, LC tanks for oscillators, etc. Since this model can be run in a very short period of time, the design cycle time can be greatly reduced compared to the time involved with other numerical EM solvers.

Bibliography

- [1] M. Niknejad and R. G. Meyer, "Design, Simulation, and Applications of Inductors and Transformers for Si RF ICs," Boston, MA: Kluwer Academic Publishers, 2000.
- [2] F. W. Grover, Inductance Calculations, New York: D. Van Norstrand Company inc., 1946.
- [3] R. Paul, Introduction to Electromagnetic Compatibility, New York, Wiley, 1992.
- [4] E. Ruehli, "Equivalent Circuit Models for Three-Dimensional Multiconductor Systems," IEEE Trans. Microwave Theory Tech., Vol. MTT-22, No. 3, pp 216-221, Mar. 1974.
- [5] M. Niknejad, R. Gharpurney, and R. G. Meyer, "Numerically Stable Green Function for Modeling and Analysis of Substrate Coupling in Integrated Circuits," IEEE Trans. Computer-Aided Design, Vol. 17, pp 305-315, Apr. 1998.
- [6] M. Niknejad and R. G. Meyer, "Analysis, Design and Optimization of Spiral Inductors and Transformers for Si RF IC's," IEEE J. Solid-State Circuits, Vol. 33, No. 10, pp 1470-1481, Oct. 1998.
- [7] H. M. Greenhouse, "Design of Planar Rectangular Microelectronic Inductors," IEEE Trans. Parts, Hybrids, and Packag., Vol. PHP-10, No. 2, pp 101-109, Jun. 1974.
- [8] W. B. Kuhn and N. M. Ibrahim, "Analysis of Current Crowding Effects in Multiturn Spiral Inductors," IEEE Trans. Microwave Theory Tech., Vol. 49, No. 1, pp 31-38, Jan. 2001.
- [9] R. Gharpurey (1995), "Modeling and Analysis of Substrate Coupling in Integrated Circuits," Ph.D dissertation, Univ. of California, Berkley.
- [10] H. Ymeri, B. Nauwelaers, K. Maex, D. D. Roest, S. Vandenberghe, and M. Stucchi, "Admittance Matrix Calculations of On-Chip Interconnects on Lossy Silicon Substrate Using Multilayer Green's Function," Silicon Monolithic Integrated Circuits in RF Systems, 2001. Digest of Papers. 2001 Topical Meeting on 12-14 Sept. 2001, pp. 50 – 59.
- [11] K. J. Idstein. (2003), "Rigorous Development of Lumped Circuit Model for Integrated Inductors," The Ohio State University Master's Thesis.
- [12] K. Idstein, R. G. Rojas, and G. Creech, "Modeling of Planar Inductors in IC's at X-Band," 2003 IEEE AP-S International Symposium and USNC/URSI National Radio Science Meeting, Columbus, OH, June 22-27, 2003.
- [13] R. G. Rojas, A. Buurma, K. Idstein, and G. Creech, "A Rigorous Approach to Lumped Element Circuit Models for Monolithic Inductors," 2004 IEEE AP-S Int'l Symposium and USNC/URSI National Radio Science Meeting, Monterey, CA, June 19-25 (invited).
- [14] R. F. Harrington, Electromagnetic Engineering, NY: McGraw-Hill, 1958, pp. 234-239.
- [15] P. Yue, S. S. Wong, "Physical Modeling of Spiral Inductors on Silicon," IEEE Trans. Electron Devices, Vol. 47, pp.560-568, Mar. 2000.
- [16] Scuderi, T. Biondi, E. Ragonese, and G. Palmisano, "A Lumped Scalable Model for Silicon Integrated Spiral Inductors," IEEE Trans. Circuits Sys. I, Vol. 51, No. 6, pp. 1203-1209, June 2004.
- [17] E. Pettenpaul, H. Kapusta, A. Weisgerber, H. Mampe, J. Luginsland, and I. Wolff, "CAD Models of Lumped Elements on GaAs up to 18 GHz," IEEE Trans. Microwave Theory Tech., Vol. 36, No. 2, pp 294-304, Feb. 1988.
- [18] P. Pathak (2004), Lecture notes – Electromagnetic Field Theory III, The Ohio State University.
- [19] Weisshaar, H. Lan, A. Luoh, "Accurate Closed-Form Expressions for the Frequency-Dependent Line Parameters of On-Chip Interconnects on Lossy Silicon Substrate," IEEE Trans. on Advanced Pack., Vol. 25, No. 2, pp 288-296, May 2002.

Appendix A: A General Approach to Solving the Electrostatic Green's Function for a Multilayered Substrate

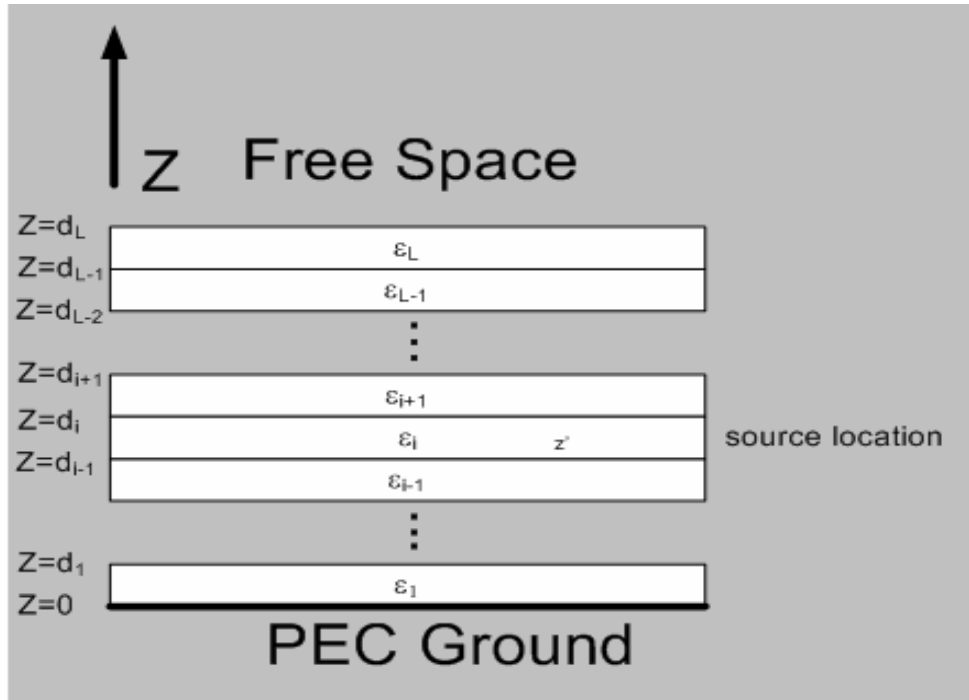


Figure 30 - Profile of L-layered substrate

With reference to [5], [10], and [18], we consider the derivation of the multilayer electrostatic Green's function, G_e , for the L-layered structure in Figure 30. The dimensions of the structure shown in Figure 30 are a in the x -direction and b in the y -direction. $G_e(r; r')$ is found by inverting Poisson's equation and gives the potential at the observation point r due to a point charge source placed at a point r' . In our case, all metal layers are in the top layer, which means both the source and observation points will be in the top layer. However, for generality we will perform the derivation assuming the source location can be in any layer.

Poisson's equation in equation (A.1) can be written in the Green's function form of equation (A.2).

$$\nabla^2 \phi = -\frac{\rho}{\epsilon} \quad (\text{A.1})$$

$$\nabla^2 G_e(r; r') = -\frac{\delta(x-x')\delta(y-y')\delta(z-z')}{\epsilon_i}, \quad (\text{A.2})$$

where the subscript i indicates the source layer. The form of G_e is

$$G_e = X(x; x')Y(y; y')Z'(z; z'). \quad (\text{A.3})$$

We substitute X , Y , and Z' into equation (A.2) which gives

$$YZ' \frac{d^2}{dx^2} X + Z'X \frac{d^2}{dy^2} Y + XY \frac{d^2}{dz^2} Z' = -\frac{\delta(x-x')\delta(y-y')\delta(z-z')}{\epsilon_i} \quad (\text{A.4})$$

The boundary condition on the side-walls of the structure in Figure 30 is $\hat{n} \bullet \vec{E} = 0$. To satisfy this, we let $X = \cos\left(\frac{m\pi}{a}x\right)$ and $Y = \cos\left(\frac{n\pi}{b}y\right)$. Plugging in the functions for X and Y we re-write equation (A.4) as

$$\sum_{m=0}^{\infty} \sum_{n=0}^{\infty} \cos\left(\frac{m\pi}{a}x\right) \cos\left(\frac{n\pi}{b}y\right) \times \left\{ \frac{d^2}{dz^2} Z' - \left[\left(\frac{m_1\pi}{a}\right)^2 + \left(\frac{n_1\pi}{b}\right)^2 \right] Z' \right\} = \frac{\delta(x-x')\delta(y-y')\delta(z-z')}{\epsilon_i} \quad (\text{A.5})$$

We multiply both sides by $\cos\left(\frac{m\pi}{a}x\right) \cos\left(\frac{n\pi}{b}y\right)$ and integrate both sides over x and y from 0 to a and 0 to b , respectively, and this gives

$$\frac{ab}{4} \left\{ \frac{d^2}{dz^2} Z' - \left[\left(\frac{m_1\pi}{a}\right)^2 + \left(\frac{n_1\pi}{b}\right)^2 \right] Z' \right\} = -\frac{\delta(z-z')}{\epsilon_i} \cos\left(\frac{m\pi}{a}x'\right) \cos\left(\frac{n\pi}{b}y'\right) \quad (\text{A.6})$$

We substitute $Z' = Z_{mn}(z; z') \cos\left(\frac{m\pi}{a}x'\right) \cos\left(\frac{n\pi}{b}y'\right)$ into equation (A.6) to simplify to

$$\frac{ab}{4} \left(\frac{d^2}{dz^2} - t_{mn}^2 \right) Z_{mn}(z; z') = -\frac{\delta(z-z')}{\epsilon_i} \quad (\text{A.7})$$

where $t_{mn}^2 = \left(\frac{m\pi}{a}\right)^2 + \left(\frac{n\pi}{b}\right)^2$. From equation (A.7) we can solve for $Z_{mn}(z; z')$ using the method of solving a one-dimensional Green's functions outlined in [18]. The method is summarized below.

A solution to equation (A.7) has the form

$$Z_{mn}(z; z') = C_k e^{t_{mn}z} + D_k e^{-t_{mn}z} \quad (\text{A.8})$$

in layer k . A recursive relation is obtained between the coefficients in adjacent layers using the boundary conditions. At the boundary between each interface, the voltage and $\hat{n} \times \vec{D}$ is

continuous. In addition, the voltage at the bottom is zero due to the ground plane. At the top, we have zero normal \vec{E} field due to the magnetic wall condition. This recursive relation can be represented by a matrix $[A]$.

$$\begin{bmatrix} C_{k+1} \\ D_{k+1} \end{bmatrix} = [A] \begin{bmatrix} C_k \\ D_k \end{bmatrix} \quad (\text{A.9})$$

where $[A]$ can be found from the boundary conditions as

$$[A] = \begin{bmatrix} \frac{1}{2} \left(1 + \frac{\epsilon_k}{\epsilon_{k+1}} \right) & \frac{1}{2} \left(1 - \frac{\epsilon_k}{\epsilon_{k+1}} \right) e^{-2t_{mn}d_k} \\ \frac{1}{2} \left(1 - \frac{\epsilon_k}{\epsilon_{k+1}} \right) e^{2t_{mn}d_k} & \frac{1}{2} \left(1 + \frac{\epsilon_k}{\epsilon_{k+1}} \right) \end{bmatrix}. \quad (\text{A.10})$$

Next, we introduce the self-adjoint operator L .

$$L = \frac{d}{dz} \left[p(z) \frac{d}{dx} \right] - q(x) \quad (\text{A.11})$$

We want a Green's function that satisfies an equation of the form

$$[L + \lambda w(z)] Z_{mn}(z; z') = -\delta(z - z') \quad (\text{A.12})$$

together with the boundary conditions

$$\alpha_{a,b} p(z) Z'_{mn}(z; z') + \beta_{a,b} Z_{mn}(z; z') \Big|_{z=a,b} = 0, \quad (\text{A.13})$$

where L is the self-adjoint operator of equation (A.11). The solution to equation (A.12) is divided into two intervals.

$$Z_{mn}(z; z') = \begin{cases} \frac{U(z)T(z')}{C} & z \leq z' \\ \frac{U(z')T(z)}{C} & z \geq z' \end{cases} \quad (\text{A.14})$$

where C is a constant and U and T are two independent solutions of

$$[L + \lambda w(z)] \frac{U(z)}{T(z)} = 0 \quad (\text{A.15})$$

with

$$\begin{aligned} \alpha_a p(z) U'(z) + \beta_a U(z) &= 0 \Big|_{z=a} \\ \alpha_b p(z) T'(z) + \beta_b T(z) &= 0 \Big|_{z=b} \end{aligned} \quad (\text{A.16})$$

and

$$C = p(z')[T(z')U'(z') - T'(z')U(z')]. \quad (\text{A.17})$$

Equation (A.16) is necessary to ensure that equation (A.13) is satisfied. To use this method for equation (A.7), we re-write it as

$$\frac{ab\varepsilon_i}{\Delta_{mn}} \left(\frac{d^2}{dz^2} - t_{mn}^2 \right) Z_{mn}(z; z') = -\delta(z - z') \quad (\text{A.18})$$

where

$$\Delta_{mn} = \begin{cases} 4 & m, n \neq 0 \\ 2 & (m = 0, n \neq 0) \text{ or } (m \neq 0, n = 0) \\ 1 & m = n = 0 \end{cases} \quad (\text{A.19})$$

To put equation (A.18) into the same form as equation (A.12), we recognize that $p(z) = \frac{ab\varepsilon_i}{\Delta_{mn}}$,

$w(z) = 1$, $q(z) = 0$, and $\lambda = -t_{mn}^2$. In addition, $\alpha_a = 0$, $\beta_a = 1$, $\beta_b = 0$, and $\alpha_b = \frac{\Delta_{mn}}{ab\varepsilon_i}$ to satisfy

the boundary conditions of equation (A.16).

We proceed with solving for $T(z)$ and $U(z')$ for $z \geq z'$. Using equation (A.8) in matrix form, we solve for $T(z)$ as

$$T(z) = \begin{bmatrix} e^{t_{mn}z} & e^{-t_{mn}z} \end{bmatrix} \begin{bmatrix} C_k \\ D_k \end{bmatrix} \quad (\text{A.20})$$

where $k \geq i$. We can find C_k and D_k using the boundary condition at $z = d_L$ in conjunction with the recursive relation, applied from the top down towards the k^{th} layer. From the boundary condition at d_L we find

$$D_L = C_L e^{2t_{mn}d_L}. \quad (\text{A.21})$$

We can set D_L to 1 since it will drop out in a ratio with D_L later on. This allows us to find $\begin{bmatrix} C_k \\ D_k \end{bmatrix}$

as

$$\begin{bmatrix} C_k \\ D_k \end{bmatrix} = [A_k]^{-1} [A_{k+1}]^{-1} \dots [A_{L-2}]^{-1} [A_{L-1}]^{-1} \begin{bmatrix} 1 \\ e^{2t_{mn}d_L} \end{bmatrix} C_L \quad (\text{A.22})$$

We plug the result for equation (A.22) into equation (A.20) to find $T(z)$. Next we need to find $U(z')$ for $z \geq z'$.

$$U(z') = \begin{bmatrix} e^{t_{mn}z'} & e^{-t_{mn}z'} \end{bmatrix} \begin{bmatrix} C_i^l \\ D_i^l \end{bmatrix} \quad (\text{A.23})$$

The superscript l in the coefficients C and D indicates that the source location z' is below the observation point z . The coefficients C_i^l and D_i^l for $U(z')$ are found in a manner similar to how the coefficients C_k and D_k were found for $T(z)$ except we start from the bottom and apply the recursive relation towards the top. From the boundary condition at $z=0$ where we have a ground plane, we can relate the coefficients C_l and D_l by plugging $z=0$ into equation (A.8) and setting $Z_{mn}(0; z') = 0$. From this we get

$$C_l = -D_l \quad (\text{A.24})$$

We can set $D_l = 1$ for the same reason we can set $D_L = 1$ previously. This gives us

$$\begin{bmatrix} C_i^l \\ D_i^l \end{bmatrix} = [A_{i-1}][A_{i-2}] \dots [A_1] \begin{bmatrix} 1 \\ -1 \end{bmatrix} C_1. \quad (\text{A.25})$$

The values for the coefficients found in equation (A.25) are then plugged into equation (A.23).

Up to this point, half of the solution to equation (A.14) has been found. The next step is to solve for $T(z')$ and $U(z)$ for the case $z \leq z'$. For this case, layer $k \leq$ layer i . $U(z)$ is found as

$$U(z) = \begin{bmatrix} e^{t_{mn}z} & e^{-t_{mn}z} \end{bmatrix} \begin{bmatrix} C_k \\ D_k \end{bmatrix}. \quad (\text{A.26})$$

The coefficients C_k and D_k are found using the recursive relation applied from the bottom layer to the k^{th} layer, with the aid of the boundary condition $Z_{mn}(0; z') = 0$.

$$\begin{bmatrix} C_k \\ D_k \end{bmatrix} = [A_{k-1}][A_{k-2}] \dots [A_2][A_1] \begin{bmatrix} 1 \\ -1 \end{bmatrix} C_1 \quad (\text{A.27})$$

Again, we plug the result of equation (A.27) into equation (A.26). $T(z')$ is found for $z \leq z'$ as

$$T(z') = \begin{bmatrix} e^{t_{mn}z'} & e^{-t_{mn}z'} \end{bmatrix} \begin{bmatrix} C_i^u \\ D_i^u \end{bmatrix} \quad (\text{A.28})$$

The superscript u in the coefficients C and D indicates that the source location z' is above the observation point z . The coefficients C_i^u and D_i^u are found by applying the recursive relation with $[A]$, starting again from the $z = d_L$, in conjunction with the boundary condition at $z = d_L$ and working downwards towards layer i . This gives

$$\begin{bmatrix} C_i^u \\ D_i^u \end{bmatrix} = [A_i]^{-1} [A_{i+1}]^{-1} \dots [A_{L-2}]^{-1} [A_{L-1}]^{-1} \begin{bmatrix} 1 \\ e^{2t_{mn}d_L} \end{bmatrix} C_L. \quad (\text{A.29})$$

Again, we plug the result of equation (A.29) into equation (A.28).

An expression for C in equation (A.14) is found using equation (A.18). However, the expression found for C would be broke into two intervals, one for $z \leq z'$ and one for $z \geq z'$. We introduce a variable \tilde{C} , as well as coefficients $C_<$, $D_<$, $C_>$, and $D_>$ to allow us to write $Z_{mn}(z; z')$ in one expression.

$$Z_{mn}(z; z') = \frac{1}{\tilde{C}} \begin{bmatrix} e^{t_{mn}z_<} & e^{-t_{mn}z_<} \end{bmatrix} \begin{bmatrix} C_< \\ D_< \end{bmatrix} \begin{bmatrix} e^{t_{mn}z_>} & e^{-t_{mn}z_>} \end{bmatrix} \begin{bmatrix} C_> \\ D_> \end{bmatrix} = G_e(z; z') \quad (\text{A.30})$$

where $z_<$ clearly means the use of z if $z < z'$ and the use of z' if $z > z'$. We also have

$$C_< = \begin{cases} C_k & k \leq i, z \leq z' \\ C_i^l & k \geq i, z \geq z' \end{cases} \quad (\text{A.31})$$

$$D_< = \begin{cases} D_k & k \leq i, z \leq z' \\ D_i^l & k \geq i, z \geq z' \end{cases} \quad (\text{A.32})$$

$$C_> = \begin{cases} C_k & k \geq i, z \geq z' \\ C_i^u & k \leq i, z \leq z' \end{cases} \quad (\text{A.33})$$

$$D_> = \begin{cases} D_k & k \geq i, z \geq z' \\ D_i^u & k \leq i, z \leq z' \end{cases}. \quad (\text{A.34})$$

The variable \tilde{C} is defined as

$$\tilde{C} = \frac{2ab\epsilon_i}{\Delta_{mn}} t_{mn} \begin{bmatrix} 1 & -1 \end{bmatrix} [A_1]^T [A_2]^T \dots [A_{i-2}]^T [A_{i-1}]^T \begin{bmatrix} 0 & 1 \\ -1 & 0 \end{bmatrix} [A_i]^{-1} [A_{i+1}]^{-1} \dots [A_{L-2}]^{-1} [A_{L-1}]^{-1} \begin{bmatrix} 1 \\ e^{2t_{mn}d_L} \end{bmatrix} \quad (\text{A.35})$$

We tested this method by applying it to the substrate under consideration in this report. For this, we set $i=j=2$ and $L=2$ since we have a two-layer substrate with both metal layers (source and observation points) in the top layer. Without getting into the details, we find $Z_{mn}(z; z')$ as follows. For $z \leq z'$,

$$Z_{mn}(z; z') = \frac{(C_2^l e^{t_{mn}z} + D_2^l e^{-t_{mn}z})(e^{t_{mn}z'} + e^{2t_{mn}d_L} e^{-t_{mn}z'})}{\frac{2ab\epsilon_i}{\Delta_{mn}} t_{mn} (C_2^l e^{2t_{mn}d_L} - D_2^l)}. \quad (\text{A.36})$$

Equation (A.36) matches the result found in [10] found for the case $z \leq z'$. For $z \geq z'$,

$$Z_{mn}(z; z') = \frac{(C_2^l e^{t_{mn} z'} + D_2^l e^{-t_{mn} z'})(e^{t_{mn} z} + e^{2t_{mn} d_L} e^{-t_{mn} z})}{\frac{2ab\varepsilon_i}{\Delta_{mn}} t_{mn} (C_2^l e^{2t_{mn} d_L} - D_2^l)}. \quad (\text{A.37})$$

This also matches the result found in [10] for the case $z \geq z'$.

The above derivation works for all values of m and n except for $m = n = 0$. We will study that case in detail in Appendix B.

Appendix B: Fast Computation of the Coefficient of Potential Matrix

The following summary of the method for obtaining the coefficient of potential matrix is done with reference to [5] and [9].

Recall the coefficient of potential matrix has elements p_{ij} , which gives the potential V_i on rectangle i due to a charge Q_j placed on rectangle j , is defined as

$$p_{ij} = \frac{1}{v_i v_j} \int_{v_i} \int_{v_j} G_e dv_j dv_i = \frac{V_i}{Q_j}. \quad (\text{B.1})$$

Because the thickness is very small relative to the surface area, we ignore the thickness of rectangles i and j and integrate over the surface, which gives

$$p_{ij} = \frac{1}{s_i s_j} \int_{s_i} \int_{s_j} G_e ds_j ds_i. \quad (\text{B.2})$$

From Appendix A we know that G_e is of the form $G_e = X(x; x')Y(y; y')Z'(z; z')$. Plugging in

$X = \cos\left(\frac{m\pi}{a}x\right)$, $Y = \cos\left(\frac{n\pi}{b}y\right)$ and $Z' = Z(z; z')\cos\left(\frac{m\pi}{a}x'\right)\cos\left(\frac{n\pi}{b}y'\right)$, we can re-write G_e

as

$$G_e = \sum_{m=0}^{\infty} \sum_{n=0}^{\infty} \left\{ \cos\left(\frac{m\pi}{a}x\right) \cos\left(\frac{n\pi}{b}y\right) \cos\left(\frac{m\pi}{a}x'\right) \cos\left(\frac{n\pi}{b}y'\right) Z_{mn}(z; z') \right\}. \quad (\text{B.3})$$

where $Z_{mn}(z; z')$ is found from equation (A.30). The set of rectangles i and j and their coordinates is given in Figure 31.

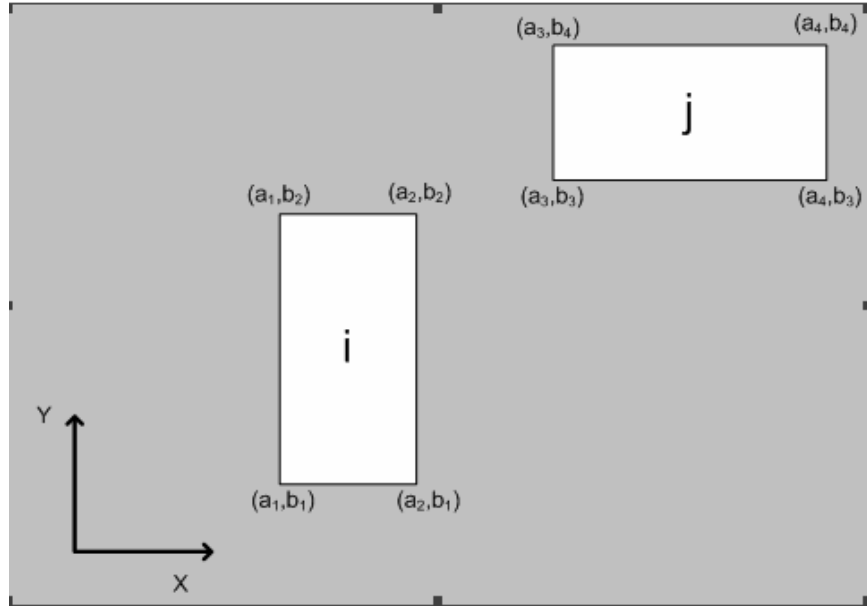


Figure 31 - Coordinates for rectangles i and j (based on [5])

Performing the integration from equation Figure 31 on the set of contacts for rectangles *i* and *j* shown in Figure 31, ignoring the $m = n = 0$ case, gives

$$p_{ij} = \sum_{m=0}^{\infty} \sum_{n=0}^{\infty} \left(\frac{\sin\left(m\pi \frac{a_2}{a}\right) - \sin\left(m\pi \frac{a_1}{a}\right)}{a_2 - a_1} \times \frac{\sin\left(m\pi \frac{a_4}{a}\right) - \sin\left(m\pi \frac{a_3}{a}\right)}{a_4 - a_3} \times \frac{\sin\left(n\pi \frac{b_2}{b}\right) - \sin\left(n\pi \frac{b_1}{b}\right)}{b_2 - b_1} \times \frac{\sin\left(n\pi \frac{b_4}{b}\right) - \sin\left(n\pi \frac{b_3}{b}\right)}{b_4 - b_3} \times Z_{mn} \right) \quad (\text{B.4})$$

The sinusoidal terms in equation (B.4) are then multiplied out and we use the identity shown in equation (B.5) to put equation (B.4) into the form of a discrete cosine transform (DCT).

$$\sin\left(m\pi \frac{a_i}{a}\right) \sin\left(m\pi \frac{a_j}{a}\right) = \frac{1}{2} \left(\cos\left(m\pi \frac{a_i - a_j}{a}\right) - \cos\left(m\pi \frac{a_i + a_j}{a}\right) \right) \quad (\text{B.5})$$

As in [5] and [9], this allows us to re-cast equation (B.4) into a sum of 64 terms *of the form*

$$\sum_{m=0}^{\infty} \sum_{n=0}^{\infty} \tilde{Z}_{mn} \cos\left(m\pi \frac{a_{1,2} \pm a_{3,4}}{a}\right) \cos\left(n\pi \frac{b_{1,2} \pm b_{3,4}}{b}\right) \quad (\text{B.6})$$

This is of the same form as a 2-D DCT. By inspection of equation (B.6), it is apparent that for the case $m = 0, n \neq 0$ or $m \neq 0, n = 0$, the form of equation (B.6) becomes the form of a 1-D DCT.

Equation (B.6) is not solvable due to the infinite upper bound on the DCT. To make equation (B.6) solvable with a DCT, we need to discretize the substrate in the x and y directions and represent the coordinates of the contacts as ratios of integers as in [5] and [9].

$$\frac{a_k}{a} = \frac{p_k}{P}, \frac{b_k}{b} = \frac{q_k}{Q} \quad (\text{B.7})$$

This allows equation (B.6) to be re-written as

$$\sum_{m=0}^{P-1} \sum_{n=0}^{Q-1} \tilde{Z}_{mn} \cos\left(m\pi \frac{p_{1,2} \pm p_{3,4}}{P}\right) \cos\left(n\pi \frac{q_{1,2} \pm q_{3,4}}{Q}\right). \quad (\text{B.8})$$

The variables a and b in equation (B.7) are the x and y dimensions of the substrate. They do not need to be the exact value, just large enough for convergence. The inductors we studied are on the order of a few hundred microns in diameter and $a=b=1024$ μm is adequate for convergence. The values of P and Q determine the number of iterations over which the infinite summations are made, or in other words, the size of the DCT.

Equation (B.8) is not exactly a DCT because of the \pm terms in the numerator which have an upper limit up to $2P$ and $2Q$. To truly be a DCT, the indices in the numerator of the cosine arguments in the DCT must not be greater than the upper limits, $P-1$ and $Q-1$ in this case. The following properties of symmetry of the DCT allow us to get around this. We define Z_{pq} as

$$Z_{pq} = \sum_{m=0}^{P-1} \sum_{n=0}^{Q-1} \tilde{Z}_{mn} \cos\left(m\pi \frac{p}{P}\right) \cos\left(n\pi \frac{q}{Q}\right) \quad (\text{B.9})$$

$$Z_{p,q} = Z_{2P-p,q} = Z_{p,2Q-q} = Z_{2P-p,2Q-q} \quad (\text{B.10})$$

Equation (B.9) is in the exact form of a P by Q DCT. Thus, if the terms $p_{1,2} \pm p_{3,4}$ and $q_{1,2} \pm q_{3,4}$ are greater than $P-1$ or $Q-1$, respectively, we can flip the values across P and Q using the identities in equation (B.10).

For the case $m = n = 0$, the portion of G_e that is a function of x and y drops out because it is equal to 1 for $m = n = 0$. Thus, equation (B.2) becomes

$$p_{ij}^{00} = \frac{1}{s_i s_j} \int_{s_i} \int_{s_j} Z_{00} ds_j ds_i. \quad (\text{B.11})$$

If we perform this integration, we find that p_{ij}^{00} is simply the Green's function for $m = n = 0$ since the integration over the contacts is in x and y while Z_{00} is a function of z only.

$$p_{ij}^{00} = G_e^{00}(z; z') = Z_{00}(z; z') \quad (\text{B.12})$$

To find Z_{00} , we inspect equation (A.18) with $t_{mn} = 0$. The solution to Z_{00} is of the form

$$Z_{00}^u = K(C_i^u z + D_i^u), \quad (\text{B.13})$$

where the superscript u indicates $z' \geq z$ as in Appendix A. For $z' \leq z$, we have

$$Z_{00}^l = K(C_i^l z' + D_i^l). \quad (\text{B.14})$$

As in [10], we find K by integrating equation (A.18) for $z = z'$ and applying the boundary condition that the potential be continuous. Doing this gives

$$K = \frac{1}{ab\epsilon_s C_i^{u,l}}. \quad (\text{B.15})$$

We choose the superscript u or l in equation (B.15) depending upon the location of z with respect to z' as done previously.

To find the values for $C_i^{u,l}$ and $D_i^{u,l}$ we use a matrix $[A]$ as in equation (A.9), but $[A]$ is defined differently for the case $m = n = 0$. If we apply the boundary conditions of continuous potential and continuous $\hat{n} \times \bar{D}$ at the interface, as well as $Z_{00}(0; z') = 0$ due to the ground plane and $\hat{n} \bullet \bar{E} = 0$ at the top of the substrate, we find $[A]$ as

$$[A] = \begin{bmatrix} \frac{\epsilon_k}{\epsilon_{k+1}} & 0 \\ \left(1 - \frac{\epsilon_k}{\epsilon_{k+1}}\right)d_k & 1 \end{bmatrix} \quad (\text{B.16})$$

We are free to set $C_l = 1$ and we must set $D_l = 0$ because of the ground plane at $z = 0$. Thus far, we have defined p_{ij} for all values of m and n . To summarize the procedure from [5] and [9], the steps for fast computation of $[P]$ are given below.

1. Input the substrate data. This includes the thickness and dielectric constants of the dielectric layers of the substrate.
2. Compute Z_{mn} as outlined in Appendix A and Z_{00} as outlined in Appendix B.
3. Compute the DCT of Z_{mn} for all cases of m and n except for $m=n=0$.
4. Read in the x and y coordinates of the corners of the rectangles comprising the current geometry and compute the equivalent integer representation as given by equation (B.7).

5. Compute equation (B.4) using equation (B.8). Recall that for $m=n=0$, use
$$p_{ij}^{00} = G_e^{00}(z; z') = Z_{00}(z; z').$$
6. Generate $[P]$ by computing all possible combinations of rectangles. For example, if we have an inductor of 20 rectangles, $[P]$ will be 20 x 20.
7. Steps 1-3 only need to be done for a given substrate. If $[P]$ needs to be recomputed for a different geometry, go to step 4.

Appendix C: Mutual Inductance Calculation

The magnetostatic Green's function, G_m , is used to calculate the partial inductance matrix $[M]$. We make the assumption that the dielectric substrate under consideration has low loss, which leads to, from equation (2.3)

$$\nabla^2 \vec{A} = -\mu \vec{J}. \quad (\text{C.1})$$

By inverting equation (C.1) and setting \vec{J} to be a dirac delta function, we get G_m . Since $\mu = \mu_0$ for all layers, G_m is

$$G_m = \frac{\mu_0}{4\pi R}. \quad (\text{C.2})$$

As discussed in Chapter 2, we find M_{ij} from G_m as

$$M_{ij} = \frac{\mu_0}{4\pi a_i a_j} \int_{a_i} \int_{l_i} \int_{a_j} \int_{l_j} \frac{d\vec{l}_i \bullet d\vec{l}_j}{|\vec{r}_i - \vec{r}_j|} da_i da_j. \quad (\text{C.3})$$

In this appendix, we will review the techniques of [2],[6], and [7] to solve equation (C.3).

We begin with the diagonal terms of $[M]$, also known as the self inductance terms. For a rectangle of thickness t , width W , and length L , we get M_{ii} to be

$$M_{ii} (nH) = 2 \times 10^{-4} \times L(\mu m) \times \left(\ln \left(\frac{2L(\mu m)}{W(\mu m) + t(\mu m)} \right) + 0.5 \right) \quad (\text{C.4})$$

The calculation of the off-diagonal terms of $[M]$, also called the mutual inductance terms, is more complicated. The calculation of the mutual inductance has two parts: the 4 dimensional integral and the dot product.

The dot product is quite simple. If the rectangles are oriented in such a way that the lengths are perpendicular, then $d\vec{l}_i \bullet d\vec{l}_j$ is zero. If the lengths are in parallel or in series, then $d\vec{l}_i \bullet d\vec{l}_j = 1$ for current in the same direction. The dot product $d\vec{l}_i \bullet d\vec{l}_j = -1$ if the current is in the opposite direction.

The calculation of the 4 dimensional integral is done in one of two ways, depending upon the relation of the center-to-center distance D and length of the rectangles L . First, we treat the rectangles as filaments with no width and the same length L and separated by a distance d . The solution to the integral of equation (C.3) for this case is

$$M' = 2 \times 10^{-4} \times L \times \left(\ln \left(\sqrt{1 + \left(\frac{L}{d} \right)^2} + \frac{L}{d} \right) - \sqrt{1 + \left(\frac{d}{L} \right)^2} + \frac{d}{L} \right). \quad (C.5)$$

where L and d is in μm and M' is in nH . If $L \gg d$, we can simplify equation (C.5) to

$$M' = 2 \times 10^{-4} \times L \times \left(\frac{d}{L} - \ln(d) + \ln(2L) - 1 \right). \quad (C.6)$$

If the width of the rectangles is not negligible, then we use the arithmetic mean distance (AMD) for the center to center distance d and the geometric mean distance (GMD) for $\ln(d)$. The AMD defined as

$$AMD = \frac{1}{6} \left| \left(d + \frac{W_2 - W_1}{2} \right)^3 - \left(d + \frac{W_2 + W_1}{2} \right)^3 - \left(d - \frac{W_2 + W_1}{2} \right)^3 + \left(d - \frac{W_2 - W_1}{2} \right)^3 \right| \quad (C.7)$$

and the GMD is

$$\begin{aligned} GMD = & -\frac{1}{2} \left(d + \frac{W_2 - W_1}{2} \right)^2 * \ln \left(d + \frac{W_2 - W_1}{2} \right) + \frac{3}{4} \left(d + \frac{W_2 - W_1}{2} \right)^2 + \\ & \frac{1}{2} \left(d + \frac{W_2 + W_1}{2} \right)^2 * \ln \left(d + \frac{W_2 + W_1}{2} \right) - \frac{3}{4} \left(d + \frac{W_2 + W_1}{2} \right)^2 \\ & + \frac{1}{2} \left(d - \frac{W_2 + W_1}{2} \right)^2 * \ln \left(d - \frac{W_2 + W_1}{2} \right) - \frac{3}{4} \left(d - \frac{W_2 + W_1}{2} \right)^2 \\ & - \frac{1}{2} \left(d - \frac{W_2 - W_1}{2} \right)^2 * \ln \left(d - \frac{W_2 - W_1}{2} \right) + \frac{3}{4} \left(d - \frac{W_2 - W_1}{2} \right)^2 \end{aligned} \quad (C.8)$$

W_2 and W_1 are the widths of the rectangles. Equation (C.6) becomes

$$M' = 2 \times 10^{-4} \times L \times \left(\frac{AMD}{L} - GMD + \ln(2L) - 1 \right). \quad (C.9)$$

The criteria for deciding when to use the filamental approximation of equation (C.5) or the GMD/AMD approximation of equation (C.9) is based upon the size of d in relation to the length of the rectangles. If $d < .5L$, the widths of the rectangles cannot be ignored and we use the GMD/AMD approximation. If $d > .5L$, we use the filamental approximation.

In general, the two rectangles will not be the same size and will sometimes have an offset. [2] gives a method for calculating the mutual inductance of two rectangles that are offset and not equal in length. There are four different possible orientations for two rectangles of arbitrary length and offset. The first is given in Figure 33.

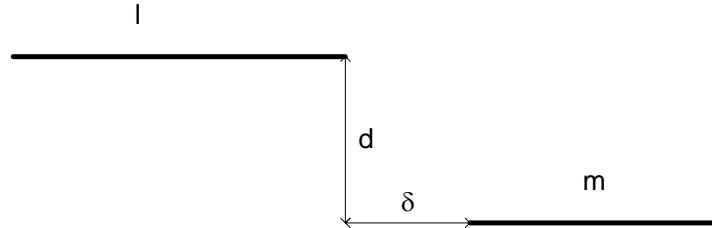


Figure 32 - Unequal parallel filaments with offset

The mutual inductance M' of the rectangles with this configuration is given as

$$M' = \frac{1}{2}(M_{l+m+\delta} + M_{\delta}) - \frac{1}{2}(M_{l+\delta} + M_{m+\delta}), \quad (C.10)$$

where the subscripts are the values for L to be used in equation (C.5) and (C.9). Equation (C.10) is for the case when the offset is positive, i.e. the filaments do not overlap. If the filaments do overlap, then we have

$$M' = \frac{1}{2}(M_{l+m-\delta} + M_{\delta}) - \frac{1}{2}(M_{l-\delta} + M_{m-\delta}). \quad (C.11)$$

If d and δ go to zero in Figure 32, we get two rectangles in series. For the case when d and δ go to zero we use

$$M' = \frac{1}{2}(M_{l+m} - M_l) - \frac{1}{2}(M_m). \quad (C.12)$$

A variation of Figure 32 is when there is a full overlap of the rectangles as shown in Figure 33.

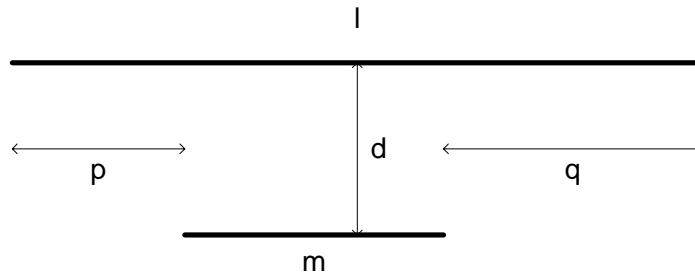


Figure 33 - Unequal parallel filaments with full overlap

The mutual inductance for the case of Figure 33 is

$$M' = \frac{1}{2} (M_{m+p} + M_{m+q}) - \frac{1}{2} (M_p + M_q). \quad (\text{C.13})$$

Lastly, there is the case when both filaments are unequal in length but have no offset as shown in Figure 34.

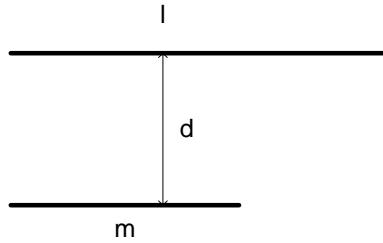


Figure 34 - Unequal parallel filaments with no offset

The mutual inductance for this case is found as

$$M = \frac{1}{2} (M_l + M_m - M_{l-m}). \quad (\text{C.14})$$